PHASE-CORRECTING DENOISING FOR DIFFUSION MAGNETIC RESONANCE IMAGING

A THESIS SUBMITTED TO

THE GRADUATE SCHOOL OF ENGINEERING AND SCIENCE

OF BILKENT UNIVERSITY

IN PARTIAL FULFILLMENT OF THE REQUIREMENTS FOR

THE DEGREE OF

MASTER OF SCIENCE

IN

ELECTRICAL AND ELECTRONICS ENGINEERING

By

Sevgi Gökçe Kafalı

April 2018

PHASE-CORRECTING DENOISING FOR DIFFUSION MAGNETIC RESONANCE IMAGING

By Sevgi Gökçe Kafalı

April 2018

We certify that we have read this thesis and that in our opinion it is fully adequate, in scope and in quality, as a thesis for the degree of Master of Science.

Emine Ülkü Sarıtaş Çukur(Advisor)

Tolga Çukur

Murat Eyüboğlu

Approved for the Graduate School of Engineering and Science:

Ezhan Karaşan
Director of the Graduate School

ABSTRACT

PHASE-CORRECTING DENOISING FOR DIFFUSION MAGNETIC RESONANCE IMAGING

Sevgi Gökçe Kafalı
M.S. in Electrical and Electronics Engineering
Advisor: Emine Ülkü Sarıtaş Çukur
April 2018

Diffusion magnetic resonance imaging (MRI) is a low signal-to-noise ratio (SNR) acquisition technique when compared to anatomical MRI. Multiple acquisitions have to be averaged to overcome this SNR problem. However, subject motion and/or local pulsations during diffusion sensitizing gradients create varying phase offsets and k-space shifts between repeated acquisitions, prohibiting direct complex averaging due to local signal cancellations in the resultant images. When multiple acquisitions are magnitude averaged, these phase issues are avoided at the expense of noise accumulation. This thesis proposes a reconstruction routine to overcome the local signal cancellations, while increasing the SNR. First, a global phase correction algorithm is employed, followed by a partial Fourier reconstruction algorithm. Then, a novel phase-correcting non-local means (PC-NLM) filtering is proposed to denoise the images without losing structural details. The proposed PC-NLM takes advantage of the shared structure of the multiple acquisitions as they should only differ in terms of phase issues and noise. The proposed PC-NLM technique is first employed on diffusion-weighted imaging (DWI) of the spinal cord, and is then modified to capture the joint information from different diffusion sensitizing directions in diffusion-tensor imaging (DTI). The results are demonstrated with extensive simulations and in vivo DWI and DTI of the spinal cord. These results show that the proposed PC-NLM provides high image quality without any local signal cancellations, while preserving the integrity of quantitative measures such as apparent diffusion coefficients (ADC) and fractional anisotropy (FA) maps. This reconstruction routine can be especially beneficial for the imaging of small body parts that require high resolution.

Keywords: Diffusion-weighted imaging, Diffusion-tensor imaging, motion, denoising, non-local means, phase correction, spinal cord.

ÖZET

DİFÜZYON MANYETİK REZONANS GÖRÜNTÜLEMEDE FAZ DÜZELTMELİ GÜRÜLTÜ GİDERİMİ

Sevgi Gökçe Kafalı
Elektrik ve Elektronik Mühendisliği, Yüksek Lisans
Tez Danışmanı: Emine Ülkü Sarıtaş Çukur
Nisan 2018

Difüzyon manyetik rezonans görüntüleme (MRG), anatomik MRG'ye kıyasla düşük sinyal-gürültü oranına (SGO) sahip bir tekniktir. SGO problemini aşmak için bir çok tekrar görüntüsünün ortalaması alınmaktadır. Ancak difüzyon ağırlıklandırmayı sağlayan gradyanlar esnasındaki hasta hareketi veya lokal pulsasyonlar, tekrar görüntüleri arasında faz farkı ve k-uzayı kaymaları yaratmakta, ve de yerel sinyal iptalleri nedeniyle karmaşık değerli ortalama alınmasını engellemektedir. Tekrar görüntülerinin mutlak değer ortalamasını almak bu faz sorunlarını engellerken gürültü birikime yol açmaktadır. Bu tezde, yerel sinyal iptalleri olmadan SGO'yu artıran bir geriçatım tekniği önerilmiştir. Öncelikle, global faz düzeltimi algoritması, ardından kısmi Fourier geriçatım tekniği uygulanmıştır. Daha sonra, yapısal detayları yitirmeden gürültüyü azaltan özgün bir "faz düzelten yerel olmayan ortalama (FD-YOO) süzgeci" önerilmiştir. Önerilen FD-YOO, tekrar görüntülerindeki ortak yapıların sadece gürültü ve de faz sorunları açısından farklı olması gerektiği bilgisinden yararlanmıştır. Önerilen FD-YOO önce difüzyon ağırlıklı MRG'de (d-MRG) uygulanmış, ardından bir çok farklı difüzyon yönüne ait benzerlik bilgisini de kullanacak şekilde difüzyon tensör MRG (dt-MRG) için değiştirilmiştir. Sonuçlar kapsamlı simulasyonlarla ve in vivo deneylerle d-MRG ve dt-MRG'de gösterilmiştir. Önerilen FD-YOO süzgeci yüksek görüntü kalitesine sinyal iptalleri olmadan ulaşabilmekte, ve de doğru difüzyon katsayısı ve fraksiyonel anizotropi değerlerine ulaşılmasını sağlamaktadır. Bu geriçatım tekniği özellikle yüksek çözünürlük gerektiren bölgelerde görüntüleme için yararlı olacaktır.

Anahtar sözcükler: Difüzyon ağırlıklı manyetik rezonans görüntüleme, difüzyon tensör manyetik rezonans görüntüleme, hareket, gürültü giderimi, yerel olmayan ortalama, faz düzeltimi, omurilik.

Acknowledgement

Due to my interest in medicine and engineering since my high-school years, the urge to have a Master's degree related to medical imaging was always growing in me. Despite this expected decision of selecting the medical imaging field as a research focus, I have definitely experienced unexpected and life changing events throughout these 3 years. Looking back at all of them, I have no regrets at all, and am very proud what I have become after this amazing time of period. I have met with numerous people that I would like to thank to, yet I have only a couple of pages to list only a few of them.

Before I start declaring the people I would like to thank to, I wish to list my funding sources. I would like to thank the following funding agencies for supporting the work in this thesis: the Scientific and Technological Research Council of Turkey through TUBITAK Grant 215E198, the European Commission through FP7 Marie Curie Career Integration Grant (PCIG13-GA-2013-618834), the Turkish Academy of Sciences through TUBA-GEBIP 2015 program, and the BAGEP Award of the Science Academy.

To start with, there is one person who is not only my supervisor but also has become my role model over the years, Dr. Emine Ülkü Sarıtaş. She deserves the most valuable thanks for this thesis work and for all the amazing advices. I have never seen a person with a greater ambition to read, discover and teach. It would be unfair not to mention the patience and tolerance she showed me when it comes to my mistakes and questions. Each and every question I asked was of importance to her. Each of my mistakes was clearly and kindly pointed out without any form of mocking or underestimation, always encouraging me to try, fail, learn and repeat. She tries to make her graduate students successfull in almost every aspect of life, with great understanding of ethics, endless ambition and serious discipline. Yet, I could not thank her enough for having a unique empathy and being able to strip away from serious supervisor attidutes when necessary. I feel very lucky to have her as my supervisor.

Throughout these 3 years, I had the chance to meet with people who I consider my best friends at the moment. Safa Özdemir is one of the most helpful and kindest people I have ever met, always with great support towards me. I must also thank him for offering snacks all the time. I also feel very fortunate to meet Mustafa Ütkür, with whom I have lots of similarities in life. It is not possible the forget his precious support and friendship. It is also very important to be able to talk to someone who went through similar academic difficulties, for which I must thank to Yavuz Muslu. I would also like to thank Koray Ertan for very informative conversations and for keeping me laughing all the time. Unlike most of the electrical engineers, I was lucky to have a female cubicle mate whom I could have girly discussions with: Cemre Arıyürek. I especially thank her for representing the small number of women in our field, together. Furthermore, I want to thank Alper Özaslan for always bringing me cookies, and for funny and interesting discussions. Lastly, I would like to thank all of my lab mates: Toygan, Burak, Rahmi, Ömer, Damla, Serhat. They all have made this journey very fun and impossible to forget at the same time.

My best friends for years, İdil Yaranlı and Özge Karaman, were always there to help me pick up my motivation and courage. I have always been inspired by them, and I am sure that our friendships will grow strong over the years. I know that we will always rock in our careers and personal lives when we stick together. Gülşah Yıldız, one of the most cheerful and relaxed people I have ever met, always knew how to have fun. In short, I will always feel very fortunate to have them in my life and I can only hope that I will have my girls beside me for many years to come.

My life partner of almost 8 years, Ayhun Tekat, was there for each and every step of my M.Sc. studies. Having someone with the different points of view in life and also in research has helped me look at from various perspectives. With his support, I was able to overcome the deepest problems and mistakes both in my research and personal life. I am more than thrilled to share my life with him and know that we have so much joy and success waiting for us in the future, together.

I would also like to thank my father, my grandmother and my grandfather who created a relaxed and fun environment at home when I needed it. I am always amazed and inspired by how hopeful they can be even during the most complicated problems. As all of them are academicians, they have always understood the issues that I faced with. Their presence throughout especially the last 3 years were incredibly helpful to me.

Most importantly, there are two people who I could not thank enough for: my sister, Göksu, and my mother. Göksu has always kept company through every struggle I had. Her bubbly and cheerful character made me feel like I can achieve anything I want in my life. I also want to thank my mom, Mehbare Özkan who I admire the most in my life. It would have not been possible to have this journey without her support, ambition and extremely useful advices. Thanks to her, I always feel how important it is to have the independence to choose your own interests. With the confidence she always gives me, now I am ready to embrace the new chapter in my life: a PhD. For all these reasons, I would like to dedicate my thesis to my mom, the most incredible and powerful woman I know. I can only wish that I can be as successfull academician as her.

Contents

List of Figures

List of Tables

Chapter 1

Introduction

Diffusion Magnetic Resonance Imaging (MRI) enables the identification of the structure and organization of tissues at the microscopic level [1, 2]. Diffusion MRI has been widely performed on the brain, but its use in small, deep regions such as the spinal cord, prostate, liver, or kidney has been relatively restricted. One of the primary limitations is reduced signal-to-noise ratio (SNR) [1], caused by the absence of custom receive-coil arrays with large number of channels that can be placed in close vicinity of these regions (as opposed to 32-96 channels for brain coils). This SNR limitation is especially problematic at high b-values and high spatial resolutions [3]. The spinal cord, for instance, has a relatively small diameter that mandates high-resolution imaging. Moreover, spine array coils typically feature only 6-8 channels and can only be placed posteriorly to the spine. In such cases, it is common to improve SNR by averaging multiple acquisitions. However, numerous sources of involuntary physiological motion complicate the averaging process [4]. Motion during diffusion-sensitizing gradients results in k-space shifts and global/local phase offsets among acquisitions. With complex averaging, these shifts/offsets can cause signal cancellations across acquisitions [5]. The most common approach to this problem in clinical settings is magnitude averaging optionally followed by image denoising. Removing phase information prevents phase-offset related issues, albeit at the expense of lower SNR [6]. Several studies considered subsequent denoising of magnitude-averaged

images to enhance diffusion MRI images and apparent diffusion coefficient (ADC) estimates [6–21]. Various denoising methods were proposed for diffusion MRI including maximum likelihood (ML) estimation [13], linear minimum mean squared error estimation [14–16], anisotropic diffusion filtering [17, 18], transform-domain denoising [21], smoothing based on constrained variational principles [19], and non-local means (NLM) filtering [9–12, 20]. Recent studies also utilized the joint information provided by diffusion MRI images in different diffusion-encoding directions, with the goal of better preserving the edges that are common across multiple images [7]. Note that these techniques were demonstrated for diffusion MRI of the brain, where higher SNR levels and reduced motion-induced problems are expected compared to the spinal cord. In relatively SNR-starved datasets, however, magnitude averaging can lead to accumulation of noise, which can be difficult to remove via post-processing approaches.

An alternative approach to improve SNR in multiple-acquisition diffusion MRI is to perform complex averaging after phase correction. This correction can be performed using a refocusing reconstruction [22] that accounts for global phase errors based on low-resolution phase information. For self-navigated acquisitions (e.g., single-shot acquisitions such as single-shot echo planar imaging (ss-EPI) or multi-shot acquisitions such as PROPELLER [23, 24]), the low-resolution phase can be extracted from a central portion of the k-space data. Other multi-shot acquisitions, on the other hand, are prone to motion-induced k-space shifts in each interleaf, requiring external navigator echoes [25, 26] or optical motion tracking [27–29]. However, correction of phase errors due to bulk motion may not compensate for local phase issues, resulting in local signal cancellations in diffusion MRI images.

This thesis proposes a reconstruction scheme for diffusion MRI that incorporates a new Phase-Correcting Non-Local-Means (PC-NLM) filter to mitigate noise and prevent local signal cancellations, while preserving the details and yielding accurate ADC and Fractional Anisotropy (FA) estimates. With this technique, both diffusion-weighted imaging (DWI) and diffusion-tensor imaging (DTI) of the spinal cord are targeted. This thesis starts with the demonstration of the local

phase issues in the spinal cord that are prominent especially when the diffusion-encoding direction has a significant component along the anterior/posterior (A/P) direction. Instead of denoising as a post-processing step, the proposed PC-NLM filter is integrated into the reconstruction routine, directly operating on multiple complex-valued acquisitions. Each acquisition is processed with a refocusing reconstruction for global phase correction and a partial k-space reconstruction via projection-onto-convex-sets (POCS). The PC-NLM filter leverages the shared structure among multiple acquisitions to simultaneously alleviate nuisance factors including phase offsets and noise. Extensive simulations and in vivo DWI/DTI experiments of the cervical spinal cord are presented. The results demonstrate that the proposed reconstruction improves image quality by mitigating signal loss due to phase offsets and reducing noise. Importantly, these improvements are achieved while preserving the accuracy of ADC and FA maps. This reconstruction can be particularly beneficial for high-resolution or high b-value DWI/DTI acquisitions that suffer from low SNR and phase offsets from local motion.

Chapter 2

Background and Theory

2.1 Diffusion MRI

Diffusion Magnetic Resonance Imaging (MRI) is a contrast mechanism that enables the measurement of the self-diffusion of excited spins [1, 2]. This self-diffusion of the spins can be modeled as a microscopic Brownian motion, where the amount of diffusion depends on the microscopic structure and the organization of the tissues, providing a unique contrast to depict various pathological changes [1]. To measure the diffusion of the spins, additional diffusion gradients are incorporated into the pulse sequence. Figure 2.1 represents two most common example pulse sequences utilized to measure the diffusion. When compared to the imaging gradients, the diffusion gradients are longer in duration (20 to 40 ms) and the amplitude is higher (20 to 40 mT/m) [1].

When a diffusion-sensitizing gradient is added into the pulse sequence, the signal from the water protons (spins) is attenuated [30]. There needs to be two diffusion gradients in the sequence to capture the amount of signal drop induced by the diffusing spins. The first diffusion-sensitizing gradient in the direction of the desired measurement will create a phase shift. According to [31], this phase

shift at $t = TE/2$ is:

$$\phi(TE/2) = \gamma \int_{t_1}^{t_1+\delta} G_d(t)x(t)dt \tag{2.1}$$

assuming that the diffusion-sensitizing gradient is applied starting from $t = t_1$ with the duration of δ. Then, a second diffusion-sensitizing gradient is applied as illustrated in Fig. 2.1. At $t = TE$, the total phase shift becomes:

$$\phi(TE) = \gamma \int_{t_1}^{t_1+\delta} G_d(t)x(t)dt - \gamma \int_{t_1+\Delta}^{t_1+\delta+\Delta} G_d(t)x(t)dt \tag{2.2}$$

If the spins are stationary, then the accumulated phases due to first and second gradient lobes will be in opposite signs with the same amount, providing a complete rephasing (i.e., $\phi(TE) = 0$). In the case of diffusing spins, rephasing is incomplete (i.e., $\phi(TE) \neq 0$) since the spins move randomly during and between the first and the second diffusion gradient lobes. As a result, each of the spins will accumulate a different phase according to its random motion path. Considering the ensemble of all spins in a voxel, the accumulated random phases of the spins will then result in an attenuated signal.

The diffusion of the spins can occur at different rates in different directions. To measure the diffusion along a specific direction, the diffusion-sensitizing gradient can be applied along that desired direction.

2.1.1 Diffusion Weighted Imaging (DWI)

As shown in Fig. 2.1, the amount of diffusion weighting can be controlled by either the amplitude or the timing of the diffusion-sensitizing gradients. By applying these gradients, the images are weighted by the diffusion coefficient of the tissue, providing a special contrast mechanism. This technique is called diffusion-weighted imaging (DWI). The diffusion-weighted signal can be modeled with the following formula;

$$S = S_0 e^{-bD} \tag{2.3}$$

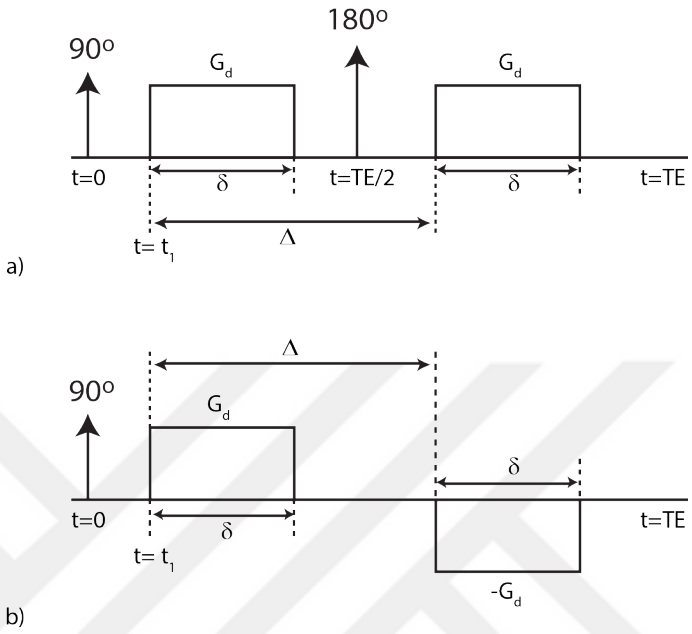

Figure 2.1: Two of the most common example pulse sequences utilized in diffusion MRI. a) Diffusion MRI pulse sequence with unipolar gradients, i.e., the spin-echo diffusion MRI sequence, b) Diffusion MRI pulse sequence with bipolar gradients, i.e., the gradient-echo diffusion MRI sequence.

where S_0 is the non-diffusion-weighted signal. $D\,[mm^2/s]$ represents the apparent diffusion coefficient (ADC) of the corresponding tissue, and $b\,[s/mm^2]$ is the so called b-value, determining the desired diffusion weighting. ADC depends on the internal kinetic energy of the spins and also the structure and the organization of the environment. For instance, if a membrane or any other barrier encircles the water protons, then the ADC gets smaller [1]. Therefore, the change in this value has the potential to detect abnormalities, such as tumor, stroke, and Alzheimer's disease [1, 3]. ADC can be computed directly from Eqn. 2.3:

$$ADC = \frac{1}{b} \ln \left(\frac{S_0}{S} \right) \tag{2.4}$$

The desired b-value can be adjusted by the duration and the amplitude of the diffusion-sensitizing gradients and directly controls the diffusion weighting. Assuming rectangular gradient lobes, the b-value can be formulated as:

$$b = (\gamma G_d \delta)^2 (\Delta - \delta/3) \tag{2.5}$$

where G_d denotes the magnitude of the diffusion gradient, δ denotes the duration of each gradient lobe, and Δ denotes the time offset between the two gradient lobes. Typical values of b ranges from 50 to 1500 s/mm^2 for brain, spinal cord, liver, and prostate imaging [1,32].

2.1.2 Diffusion Tensor Imaging (DTI)

DWI assumes that the diffusion of the spins is isotropic, meaning that the rate of diffusion is equal at every direction, as shown in Fig. 2.2a. However, biological tissues have boundaries and membranes that prevent the molecules from diffusing at equal rate in each direction. Thus, real life conditions force the diffusion to be anisotropic. This phenomenon can be modeled as a diffusion ellipsoid, as depicted in Fig. 2.2b.

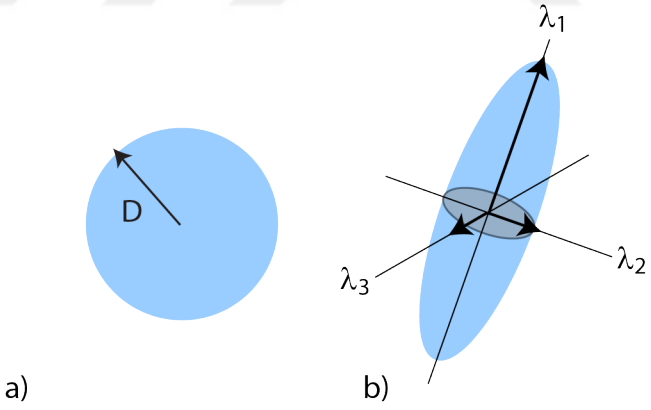

Figure 2.2: a) DWI assumes that the molecules diffuse isotropically with the rate of D at every direction. b) DTI, on the other hand, provides a more realistic model assuming an anisotropic diffusion over different directions. λ_1, λ_2, and λ_3 illustrate the rate of diffusion in 3 principal axes.

In this case, diffusion is not represented by a single coefficient of D, but a diffusion tensor D, which is a symmetric and positive definite 3×3 matrix. This matrix can be formulated as;

$$D = \begin{bmatrix} D_{xx} & D_{xy} & D_{xz} \\ D_{xy} & D_{yy} & D_{yz} \\ D_{xz} & D_{yz} & D_{zz} \end{bmatrix} \tag{2.6}$$

This MRI imaging technique with a more sophisticated and realistic understanding of diffusion is called diffusion tensor imaging (DTI). To measure the diffusion tensor, D, at least six diffusion-weighted measurements in different directions and one non-diffusion-weighted measurement must be acquired [1]. Therefore, the minimum number of required measurements of a DTI pulse sequence is seven, which makes the scan time significantly longer. By increasing the number of the directions measured, the accuracy of the diffusion tensor estimation can be increased, at the expense of prolonged scan times. Two of the main DTI-related metrics that help in the diagnosis of pathologies are:

- Mean diffusivity (MD), which is a measure of the average diffusion rate
- Fractional anisotropy (FA), which shows how anisotropic the diffusion is in a particular tissue or organ

The FA value is calculated from the eigenvalues, i.e., $\lambda_1, \lambda_2, \lambda_3$, of the corresponding diffusion tensor, D:

$$FA = \sqrt{\frac{3}{2}} \sqrt{\frac{(\lambda_1 - \lambda)^2 + (\lambda_2 - \lambda)^2 + (\lambda_3 - \lambda)^2}{\lambda_1^2 + \lambda_2^2 + \lambda_3^2}} \tag{2.7}$$

where λ is the mean of the eigenvalues, (i.e., equal to MD), $\lambda = (\lambda_1 + \lambda_2 + \lambda_3)/3$.

λ_1, λ_2, and λ_3 denote the diffusivities in 3 orthogonal directions of the diffusion ellipsoid, as shown in Fig. 2.2b. In the case of isotropic diffusion where the diffusion occurs in equal amounts in every direction, the FA value will be 0. In contrast, an FA value of 1 means that the diffusion is strictly along one direction. Calculating the FA value for each voxel in the image, an FA map can be generated. The FA maps can be visualized both in grayscale, and in color. The standard color codes for FA maps are as follows: [red, green, blue] = [Right/Left, Anterior/Posterior, Superior/Inferior].

2.2 Signal-to-Noise Ratio (SNR) Limitations in Diffusion MRI

The diffusion-weighted signal intensity mainly depends on b and D as shown in Eqn. 2.3. When a diffusion weighting is applied ($b \neq 0$), the SNR is always lower than that of the T2-weighted image (i.e., $b = 0$ image), as exemplified in Fig. 2.3a. To give a mathematical intuition, the diffusion coefficient of the gray matter is $D \approx 900 \times 10^{-6}\, mm^2/s$ and white matter has $D \approx 700 \times 10^{-6}\, mm^2/s$ on average [33]. The resultant diffusion-weighted image will have approximately 0.55 of the signal intensity of the T2-weighted image when a typical b-value of $b = 700\, s/mm^2$ is utilized (i.e.,$e^{-bD} \approx 0.55$).

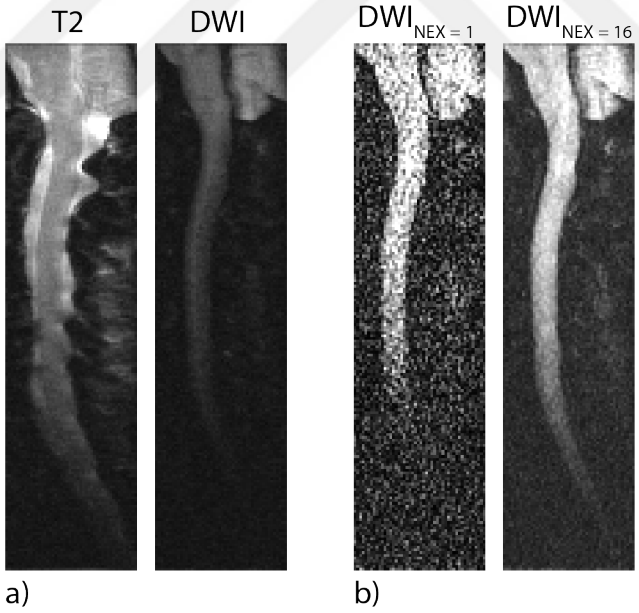

Figure 2.3: Comparison of signal levels. For each subfigure, the images are displayed with identical gray-scale windowing. a) DWI signal level is significantly lower than the T2-weighted signal level. b) To obtain a reasonable SNR, multiple acquisitions have to be averaged in DWI. NEX= 1 image fails to provide a high-quality image, whereas averaging of NEX= 16 acquisitions provides 4 times increased SNR.

As diffusion MRI is intrinsically a low-SNR acquisition, the reduced SNR is one of the primary limitations [1]. The imaging of small body parts that require high resolution (e.g., spinal cord, liver, and prostate) complicates the process even further due to the absence of custom receive-coil arrays with large number of channels that can be placed in close vicinity of these regions (as opposed to 32-96 channels for brain coils). This SNR limitation is especially problematic at high b-values and high spatial resolutions [3]. In such cases, it is common to improve SNR by averaging multiple acquisitions (NEX) to attain a reasonable SNR, as shown in Fig. 2.3b.

2.3 Motion-Induced Phase Issues in Diffusion MRI

The most challenging aspect of diffusion MRI is its motion sensitivity. Since diffusion MRI is sensitive to microscopic motion of the spins, any motion of the body far from a microscopic motion constitutes large errors in the resultant images. According to [5], the rigid body motions can be modeled as translations and rotations, and they produce zeroth- and first-order phase errors, respectively. In order to prove that, two coordinate systems are suggested:

1. (X, Y, Z) : This coordinate system is the gradient frame, i.e., X, Y, Z can be the read-out, phase-encode, and slice-select directions, respectively. The origin is defined as (X_0, Y_0, Z_0). Any point can be specified as $\vec{R} = X\hat{X} + Y\hat{Y} + Z\hat{Z}$, where $\hat{X}, \hat{Y}, \hat{Z}$ denote the coordinate unit vectors.

2. (x, y, z) : This coordinate system is the body frame. Any point can be specified as $\vec{r} = x\hat{x} + x\hat{x} + z\hat{z}$ where $\hat{x}, \hat{y}, \hat{z}$ denote the coordinate unit vectors.

The motions, i.e., rotations and translations, occur at the gradient frame, while there is no patient motion in the body frame. These two coordinate frames are

related with the following equation:

$$\vec{R} = X_0\hat{X} + Y_0\hat{Y} + Z_0\hat{Z} + \vec{r} \tag{2.8}$$

Assuming that the gradient and body frame coincide at the beginning, any motion can be written in the following form;

$$\vec{R}\,(t) = \vec{R_0}\,(t) + \vec{\theta}\,(t) \times \vec{r}\,(t) \tag{2.9}$$

where $\times$ denotes the cross product, $\vec{R_0}\,(t)\,, \vec{\theta}\,(t)$ denote the change in the origin and orientation of the body frame, respectively. $\vec{R_0}(t)$ corresponds to translation in the body frame, and the $\vec{\theta}(t)$ consists of $\theta_x(t), \theta_y(t)$, and $\theta_z(t)$ which correspond to rotation in three orthogonal directions in units of radians. In total, any motion can be modeled with six parameters: $[X_0(t), Y_0(t), Z_0(t)]$ and $[\theta_x(t), \theta_y(t), \theta_z(t)]$.

Here, $p(x, y)$ is the transverse magnetization. In case of no translation and rotation, the ideal k-space signal can be written in the following form;

$$S\,(K_x, K_y) = \int p\,(x, y)\, e^{i(K_x x + K_y y)}\, dx\, dy\, dz \tag{2.10}$$

In case of translation or rotation, signal equation can be written with an additional phase term, $\Phi\,(x, y, z)$:

$$S\,(K_x, K_y)_{corrupted} = \int p\,(x, y)\, e^{i\Phi(x,y,z)} e^{i(K_x x + K_y y)}\, dx\, dy\, dz \tag{2.11}$$

where this additional phase term is due to motion. The effect of this additional phase term can further be stated as:

$$\Phi(x, y, z) = \gamma \int \vec{G_d}(t) \cdot \vec{R}(t) dt \tag{2.12}$$

where $\cdot$ and $\vec{G_d}(t)$ denote the dot product and diffusion-sensitizing gradient, respectively. Incorporating Eqn. 2.9 to Eqn. 2.12, $\Phi\,(x, y, z)$ becomes

$$\Phi(x, y, z) = \gamma \int \vec{G_d}(t) \cdot \vec{R_0}(t) dt + [\gamma \int \vec{G_d}(t) \times \vec{\theta}(t) dt] \cdot \vec{r} \tag{2.13}$$

Equation 2.13 can be simplified as:

$$\Phi(x, y, z) = \phi_x + \phi_y + \phi_z + \vec{dk} \cdot \vec{r} \tag{2.14}$$

where $\phi_x + \phi_y + \phi_z = \gamma \int \vec{G}_d(t) \cdot \vec{R}_0(t)dt$ term is due to translation, while $\vec{dk} \cdot \vec{r}$ term is due to rotation with $\vec{dk} = \gamma \int [\vec{G}_d(t) \times \vec{\theta}(t)]dt$. These two main terms can be partitioned in terms of three orthogonal directions x, y, z:

$$dk_x = \gamma \int \left(G_{dy}(t)\, \theta_z(t) - G_{dz}(t)\, \theta_y(t) \right) dt \tag{2.15}$$

$$dk_y = \gamma \int \left(G_{dz}(t)\, \theta_x(t) - G_{dx}(t)\, \theta_z(t) \right) dt \tag{2.16}$$

$$dk_z = \gamma \int \left(G_{dx}(t)\, \theta_y(t) - G_{dy}(t)\, \theta_x(t) \right) dt \tag{2.17}$$

$$\phi_x = \gamma \int G_{dx}(t)\, X_0(t)\, dt \tag{2.18}$$

$$\phi_y = \gamma \int G_{dy}(t)\, Y_0(t)\, dt \tag{2.19}$$

$$\phi_z = \gamma \int G_{dz}(t)\, Z_0(t)\, dt \tag{2.20}$$

Therefore the resultant k-space becomes;

$$S(K_x, K_y)_{corrupted} = e^{i(\phi_x+\phi_y+\phi_z)} \int p(x,y)\, e^{i((K_x+dk_x)x+(K_y+dk_y)y)} dxdy \int e^{(idk_z z)} dz \tag{2.21}$$

$$S(K_x, K_y)_{corrupted} = e^{i(\phi_x+\phi_y+\phi_z)} S(K_x + dk_x, K_y + dk_y) \int e^{(idk_z z)} dz \tag{2.22}$$

Therefore, in the case of rotation and translation, the data in k-space is shifted by some amount, and multiplied by a phase offset. While multiplication by a global phase factor can correct for the effects of translation, it cannot correct for rotation [5]. In order to get rid of the rotation effect, a counter shift in k-space is required, which is equivalent to the multiplication of the image by a linear phase ramp. To overcome this shifting problem, a technique called "navigator echo imaging" is proposed by various studies [30]. A navigator echo mainly samples either a symmetric and a small portion of the k-space center, or only one line ($k_y = 0$) of the k-space just after/before the imaging echo. Alternatively, for single-shot imaging sequences, the required k-space shift can be computed directly from the central region of acquired k-space data itself.

2.3.1 Global Phase Correction: Refocusing Reconstruction

Refocusing reconstruction is a non-linear phase correction based on least-squares estimation [22]. Refocusing reconstruction uses a low-resolution 2D navigator data, or the central part of the acquired single-shot k-space data, to extract the information about the phase corruption of each acquisition. $S(K_x, K_y)$ is the acquired k-space data, and $W(K_x, K_y)$ is the windowing function that selects the central portion of the k-space.

$$s_c(x, y) = FFT^{-1}\{S(K_x, K_y)W(K_x, K_y)\} \tag{2.23}$$

$$p_c(x, y) = e^{i\angle s_c(x,y)} \tag{2.24}$$

where $s_c(x, y)$ is the low-resolution image from which the phase corruption is extracted.

$$s(x, y) = FFT^{-1}\{S(K_x, K_y)\} \tag{2.25}$$

where $s(x, y)$ is the phase-corrupted image. The corrected k-space data is expressed as:

$$S^{'}(K_x, K_y) = FFT\{s(x, y){p_c}^*(x, y)\} \tag{2.26}$$

where the conjugate of the phase is multiplied with the phase-corrupted image to obtain the phase-corrected image. This process can be implemented for each of the multiple acquisitions individually. Figure 2.4 shows the magnitude and phase images of multiple acquisitions when these acquisitions are not processed with any global phase correction algorithm. When these multiple acquisitions are direct complex averaged wihout any global phase correction, the resultant image yields severe signal losses (see Fig. 2.4b). As shown in Fig. 2.4c, refocusing reconstruction solves the global phase issues, and leads to image with improved image quality. On the other hand, the local phase issues, which correspond to local tissue movement during the diffusion-sensitizing gradients, cannot be resolved using this global phase correction technique, as depicted with red arrows in Fig. 2.4c.

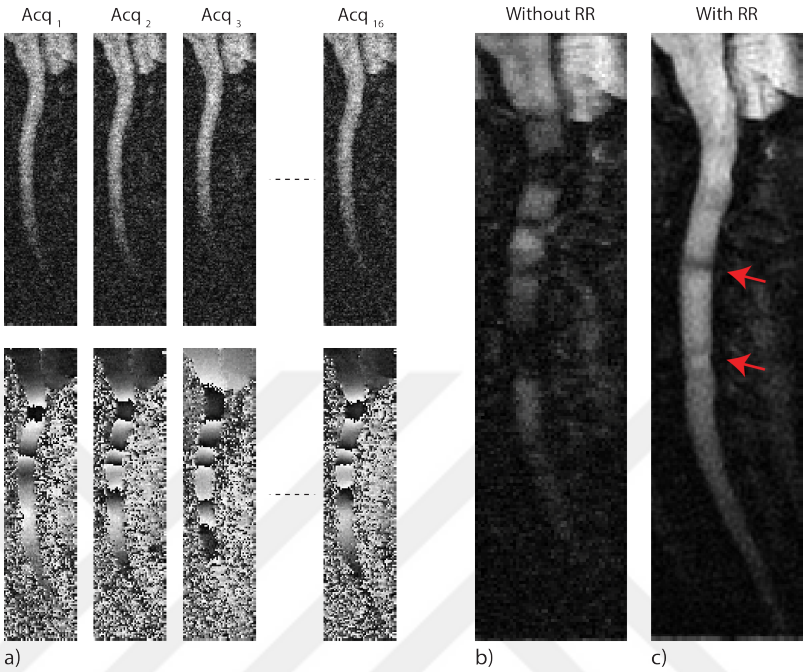

Figure 2.4: a) Magnitude and phase of each of the multiple acquisitions before refocusing reconstruction (RR). b) Complex averaging of these multiple acquisitions without refocusing reconstruction. See the signal loss in the resultant image. c) Refocusing reconstruction corrects for the global phase issues individually for each of the multiple acquisitions. When these acquisitions are complex averaged after a refocusing reconstruction, the resultant image is significantly improved when compared to (b). On the other hand, refocusing reconstruction cannot correct for the local phase issues stemming from local tissue movements such as cerebrospinal fluid pulsations (as shown with red arrows).

2.4 Drawbacks of the Current Techniques

It is common to use averaging to attain a reasonable SNR in diffusion MRI, as explained in Section 2.2. Two different approaches can be undertaken when combining multiple DWI acquisitions: global phase terms can be corrected using an algorithm such as refocusing reconstruction [22] prior to complex averaging, or phase information can be neglected entirely via magnitude averaging. The shortcomings of both approaches are exemplified in Fig. 2.5.

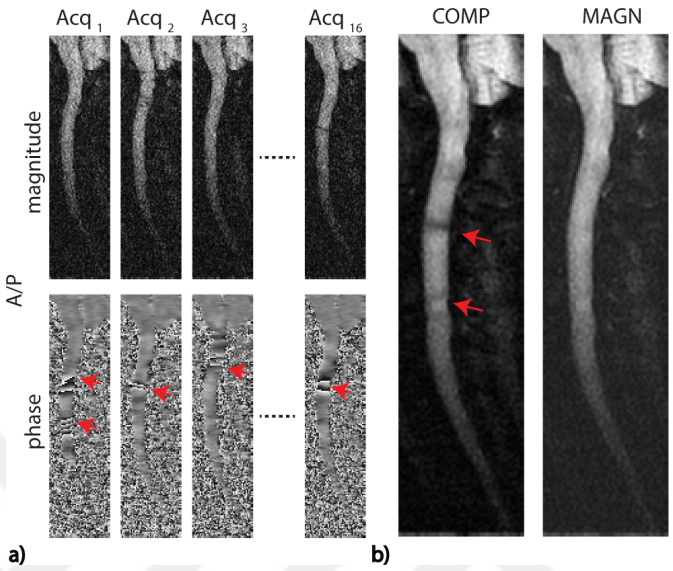

Figure 2.5: Local phase problems in DWI of the cervical spinal cord. a) Magnitude and phase of each acquisition for a single slice, following a refocusing reconstruction to correct for global phase errors and a partial k-space reconstruction. Local phase errors (shown by red arrows) are especially prominent in the case where diffusion sensitizing gradients are in the A/P direction, as in this example. b) When direct complex averaged, the phase errors result in local signal cancellations. Magnitude averaging, on the other hand, leads to an accumulation of noise especially in regions that were SNR-starved prior to averaging.

Figure 2.5a shows the magnitude and phase images of repetitions for diffusion MRI of the cervical spine. Despite global phase correction, each acquisition displays different patterns of local phases (red arrows). These local phase errors occur at exactly the same position for images obtained from all receive-array channels, indicating that they in fact stem from anatomical sources, as shown in Fig. 2.6.

In diffusion MRI of the spinal cord, the local phase issues are most prominent when the diffusion-encoding direction has a significant component along the A/P directions as shown in Fig. 2.7 and Fig. 2.8, and their locations coincide with the nerve roots exiting the spinal cord. This observation indicates a local motion of the cord in the A/P direction, which is consistent with the literature on nerve root pulsations in the same direction, synchronized to heart and cerebrospinal fluid (CSF) pulsations. Literature suggests that the local motion of the spinal cord is especially affected by the motion in the radicular arteries due to arterial

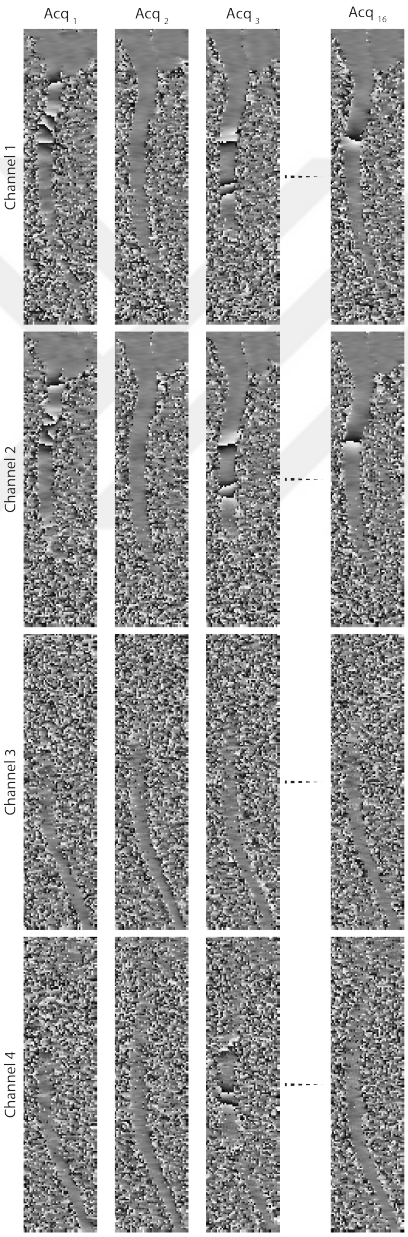

Figure 2.6: Phase images from each acquisition for the case when diffusion-encoding is along the A/P direction. Four out of 16 acquisitions are displayed explicitly. For each acquisition, phase images from 4 channels out of 6 are displayed following a refocusing reconstruction to correct for global phase errors and a partial k-space reconstruction (the remaining 2 channels are not shown as they contained noise only). These local phase problems occur at exactly the same position for images obtained from all receive channels, indicating that they in fact stem from anatomical sources.

pulsation and respiration [34–37].

As shown in Fig. 2.5b, for complex averaging following global phase correction, local phase errors can result in signal cancellations along the spinal cord. These cancellations can be mistaken with local increases in diffusion. Magnitude averaging, on the other hand, can cause noise amplification in the combined image when each repetition is SNR-starved. The goal of this thesis is to simultaneously correct for phase errors while boosting the SNR of the combined image.

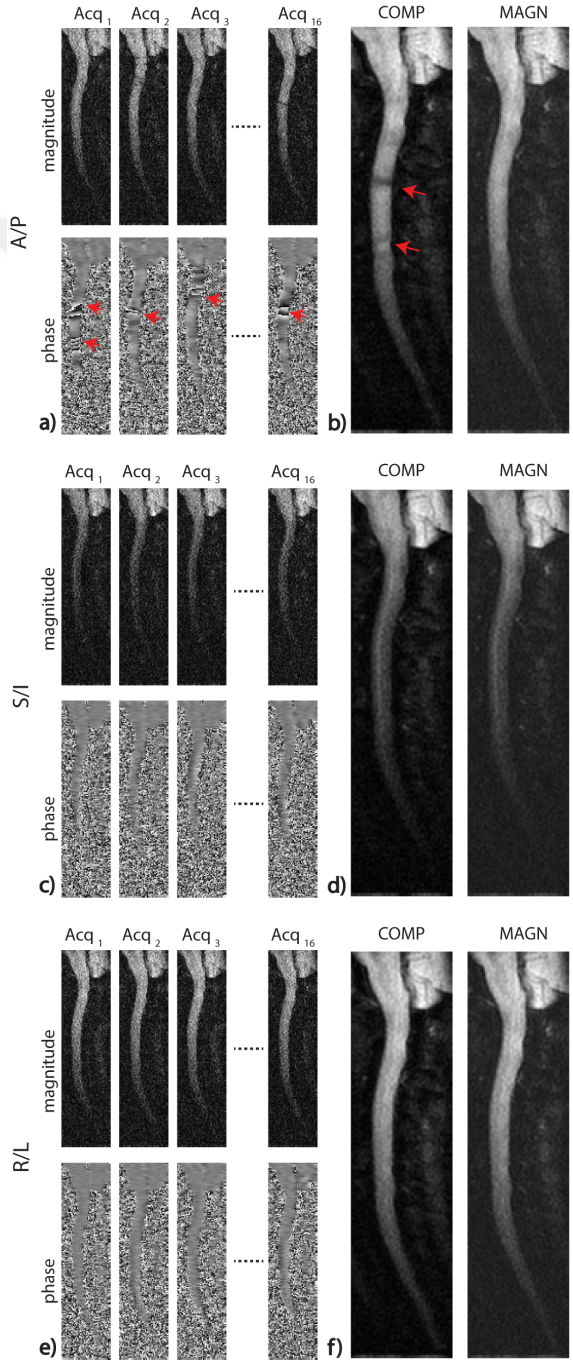

Figure 2.7: Local phase problems in DWI of the cervical spine for different diffusion-encoding directions. a,c,e) Magnitude and phase of each acquisition when diffusion-encoding is along A/P, S/I, and R/L directions, displayed following a global phase correction and a partial k-space reconstruction. b,d,f) The results of complex averaging (COMP) and magnitude averaging (MAGN) across multiple acquisitions. MAGN results in noise accumulation for all diffusion encoding directions. COMP, on the other hand, suffers from signal cancellations due to local phase problems (shown by red arrows), which are prominent when the diffusion-encoding is along the A/P direction. These phase problems occur at the positions where the nerve roots exit the spinal cord, which is consistent with the literature on nerve root pulsations in the same direction, synchronized to heart and CSF pulsations.

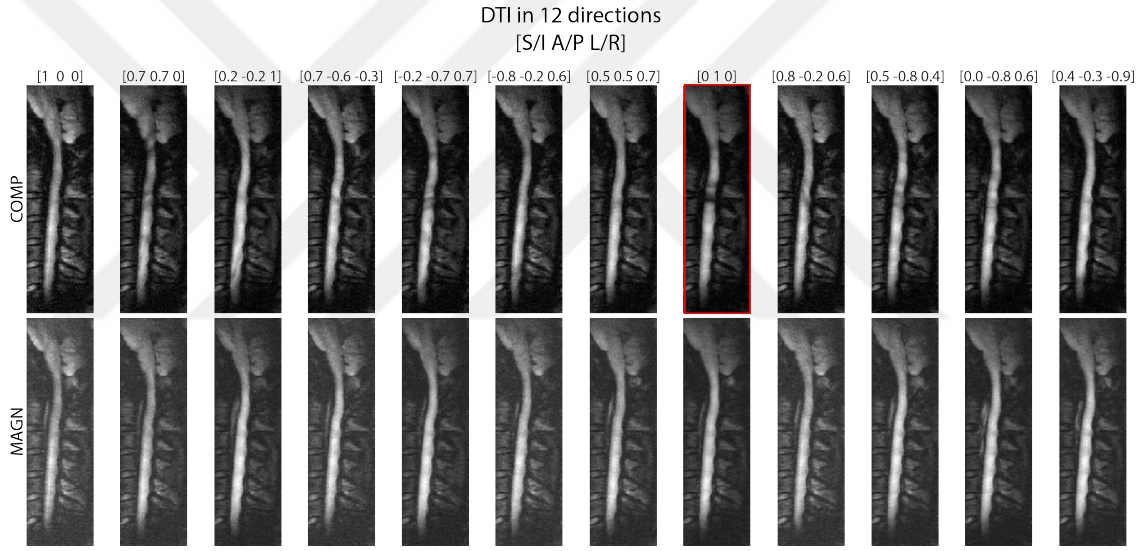

Figure 2.8: Diffusion-weighted images from DTI of the spinal cord in 12 different directions. The results are shown for complex averaging (COMP) and magnitude averaging (MAGN). The vectors on top of the images indicate the direction of diffusion encoding: [S/I A/P R/L], respectively. It is observed that while local signal cancellations are visible in many of the images, they are most prominent when the diffusion-encoding direction has a significant component along the A/P direction (e.g., [0 1 0] case displayed in red box).

Chapter 3

Phase-Correcting Non-Local Means Filtering for DWI

This chapter is based on the publication titled 'Kafali SG, Çukur T, Saritas EU. Phase-correcting non-local means filtering for diffusion-weighted imaging of the spinal cord'. Magn Reson Med. 2018; DOI: 10.1002/mrm.27105.

In this section, a description of the standard Non-Local Means (NLM) filtering is provided. Then, the proposed Phase-Correcting Non-Local Means (PC-NLM) filter and its integration into the overall image reconstruction scheme are explained. Instead of post-processing a reconstructed DWI image via NLM filtering, a novel PC-NLM filter is incorporated into the image reconstruction process to correct for phase errors while boosting SNR.

3.1 Non-Local Means (NLM) Filtering in MRI

Unlike typical denoising methods that perform filtering across small neighborhoods of pixels [38], NLM filtering denoises each pixel by averaging it with other

pixels from highly similar patches. The search for similar patches can be performed over the whole image or a specified search area [20]. Here, the standard 2D NLM filter is described with the following notations:

- $m(x_i, y_i)$: the central-pixel intensity at location (x_i, y_i).
- N_i : the local 2D neighborhood centered around (x_i, y_i), of size $(2d+1)^2$, $d \epsilon \mathbb{N}$.
- $m(N_i)$: the neighborhood intensity vector containing the intensities of the pixels inN_i.
- S_x, S_y : the sizes of the image in x- and y-directions.
- Ω^2 : the image grid.
- $|\Omega^2| = S_x S_y$: the total number of pixels in the 2D image.
- V_i : the search volume centered around (x_i, y_i), of size $(2M+1)^2$, $M \epsilon \mathbb{N}$.

The filtered intensity is a weighted average of all the pixels in the search area:

$$m_{NLM}(x_i, y_i) = \sum_{(x_j, y_j) \epsilon V_i} w(x_i, y_i; x_j, y_j) m(x_j, y_j) \tag{3.1}$$

Instead of using the distance from the central pixels, the filter weights, $w(x_i, y_i; x_j, y_j)$, are determined using the similarity between the neighborhood intensity vectors:

$$w(x_i, y_i; x_j, y_j) = \frac{1}{Z_i} e^{-\frac{|m(N_i) - m(N_j)|^2}{h^2}} \tag{3.2}$$

Here, $h \epsilon \mathbb{R}$ is a smoothing parameter calculated according to the noise variance in the image. Z_i is a normalization constant, which ensures that the sum of all filter weights is equal to one, i.e.,

$$\sum_j w(x_i, y_i; x_j, y_j) = 1 \tag{3.3}$$

As in all denoising methods, there is a trade-off between the sharpness and SNR of the resulting image. In NLM, this trade-off is controlled via h, which needs to be tuned carefully. This parameter can be estimated from the pseudo-residuals as follows [39, 40]:

$$\epsilon_i = \sqrt{\frac{4}{5}}|m(x_i, y_i) - \frac{1}{4}\sum_{x_j, y_j \epsilon P_i} m(x_j, y_j)| \tag{3.4}$$

P_i is the 4-neighborhood for pixel (x_i, y_i) and the constant $\sqrt{\frac{4}{5}}$ is used to satisfy $E[\epsilon_i^2] = \sigma^2$ [20]. Then the noise variance in the image can be estimated as:

$$\sigma^2 = \frac{1}{|\Omega^2|}\sum_{i \epsilon \Omega^2} \epsilon_i^2 \tag{3.5}$$

Finally, the smoothing parameter can be calculated by:

$$h^2 = 2\beta\,\sigma^2\,|N_i| \tag{3.6}$$

where $\beta \epsilon \mathbb{R}$ is manually tuned between 0.5 and 1, in correlation with the noise level [20].

3.2 Phase-Correcting Non-Local Means (PC-NLM) Filtering

The proposed method relies on the fact that multiple acquisitions (NEX) of the same image share the same underlying structure, but have varying phase errors and noise. To leverage this property, multiple acquisitions are first concatenated to form a large image of size $S_x \times (NEX\,S_y)$. This concatenation is performed using complex-valued images. The search volume of NLM is expanded to include patches in identical locations across repeated acquisitions, as demonstrated in Fig. 3.1a. Accordingly, if the original search volume for pixel (x_i, y_i) is $V_i(x_i, y_i)$, the expanded search volume can be expressed as:

$$V_i' = \bigcup_{n=1}^{NEX} V_i(x_i, mod(y_i + nS_y, NEX\,S_y)) \tag{3.7}$$

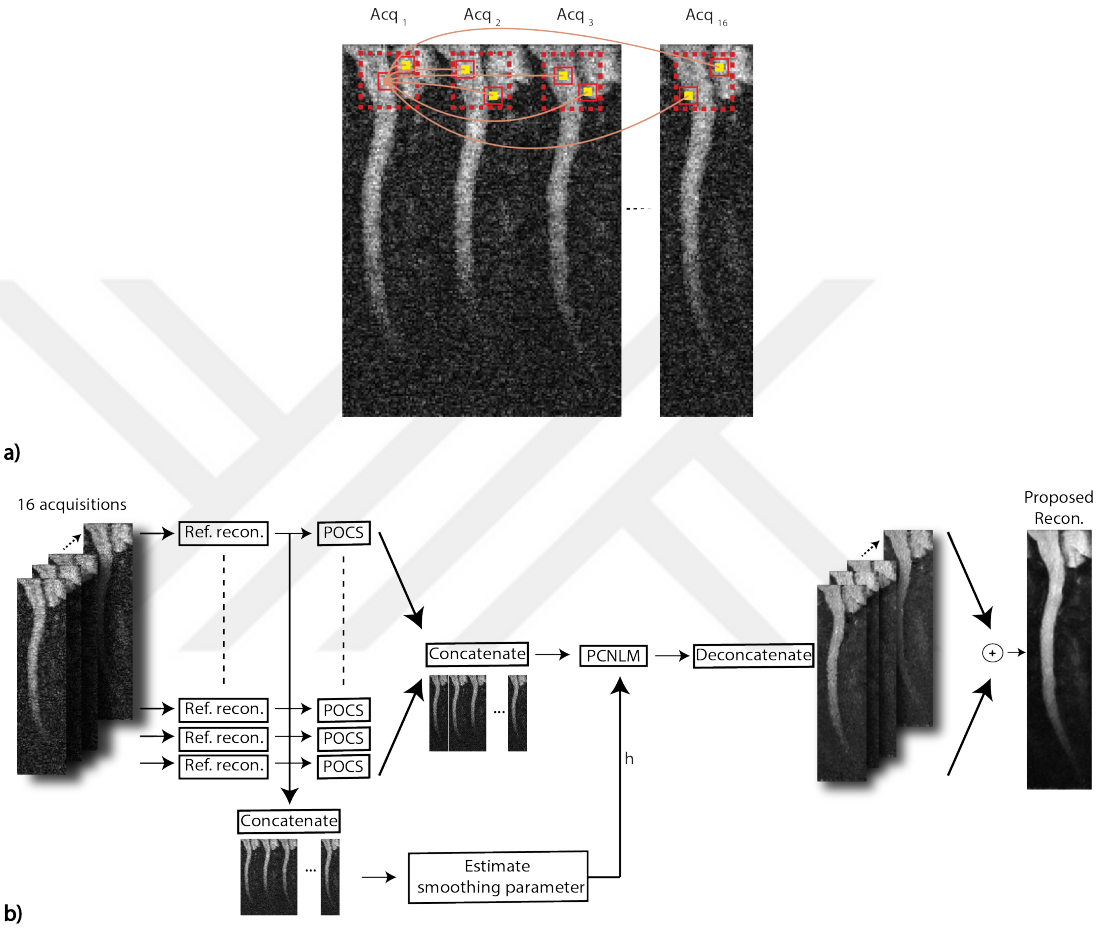

Figure 3.1: The proposed phase-correcting non-local means (PC-NLM) filter and the overall image reconstruction scheme. a) Multiple image acquisitions are first concatenated to form an aggregate image. The search volume in PC-NLM for finding similar neighborhoods is expanded to include the repeated positions across multiple acquisitions. b) The proposed reconstruction (illustrated for a single coil): multiple acquisitions are first phase-corrected via a refocusing reconstruction using a central portion of k-space data. After phase correction, individual-acquisition images are processed with the POCS algorithm (3 iterations) for partial k-space reconstruction. The complex-valued outputs of the POCS algorithm are concatenated to form an aggregate image that is processed with the PC-NLM filter. The smoothing parameter of PC-NLM is calculated from concatenated phase-corrected acquisitions to retain sensitivity for detailed image features. The filtered aggregate image is deconcatenated and magnitude averaged across acquisitions.

In the absence of phase errors, the repeated positions in the concatenated image should yield very high similarity to the neighborhood N_i of a central pixel. These positions will be effectively complex averaged during the weighted averaging step. In the presence of phase errors, however, the Euclidian distance $|m(N_i) - m(N_j)|$ will be large due to phase differences among repetitions, reducing the contribution of those positions. In this manner, phase-dependent averaging will suppress signal cancellations stemming from local phase errors. The primary goal of the PC-NLM filter is to correct for phase errors, while preserving the structural integrity of the reconstructed image. It is also important that the algorithm runs without user intervention. First, to avoid excessive denoising that may result in spatial blurring, $\beta = 0.5$ is utilized in this thesis. Next, the smoothing parameter is determined automatically using Eqn. 3.6, with a slight modification as explained in the following subsection. Here, the smoothing parameter controls not only the similarity threshold among the neighborhood intensities, but also the tolerable range of phase errors. If the smoothing parameter is set too large, averaging will be performed across many patches, causing spatial blurring. If this parameter is set too small instead, averaging will be performed across only a few patches, compromising noise suppression. Therefore, the smoothing parameter must be set to avoid excessive blurring, while allowing sufficient averaging to take place.

3.3 Image Reconstruction with PC-NLM Filtering

The proposed image reconstruction, outlined in Fig. 3.1b, corrects for global phase issues and reduces the noise level when combining multiple acquisitions. First, multiple acquisitions are phase-corrected using a refocusing reconstruction that estimates the global phase using a fully-sampled central portion of k-space data [22] (ranging between 6%-12% in this thesis). These individual phase-corrected acquisitions are then separately processed with the POCS (Projection-Onto-Convex-Sets) algorithm for partial k-space reconstruction with

3 iterations [41]. The complex-valued outputs of the POCS algorithm are concatenated across acquisitions to form an aggregate image, which is then processed with the PC-NLM filter. The neighborhood size and search volume are set to $d = 1$ and $M = 5$, as these values were previously shown to yield the lowest root-mean-squared error between ideal noise-free images and NLM-filtered noisy images [20]. Finally, the output of the PC-NLM filter is deconcatenated, and the resulting images are magnitude averaged across acquisitions. The proposed reconstruction is performed individually for each coil, and the coil images are combined via square-root of sum-of-squares.

For a conventional NLM filter, the smoothing parameter would be calculated using the image that is input to the filter (i.e., the aggregate image at the output of the POCS algorithm in this case). However, POCS amplifies high-frequency noise while filling unacquired k-space, and this can lead to overestimation of the smoothing parameter that depends on the estimated noise. Here, the smoothing parameter is instead estimated directly on global-phase-corrected acquisitions concatenated across acquisitions (see Fig. 3.1b). This estimation procedure increases sensitivity for detailed image features in the subsequent PC-NLM step.

3.4 DWI Simulations

Simulations were performed using the spinal cord MRI data extracted from PropSeg Spinal Cord Segmentation Toolbox [42, 43]. A sample T2-weighted sagittal image provided in the toolbox is shown in Fig. 3.2a (original field-of-view (FOV)= $264 \times 384\, mm^2, TE = 119\, ms, TR = 1500\, ms, 1 \times 1\, mm^2$ in-plane resolution).

The original FOV was reduced to a smaller FOV of $110 \times 54\, mm^2$ to approximate the in vivo images acquired in this work. PropSeg Toolbox was used to obtain segmented tissue masks of CSF, gray matter (GM), and white matter (WM). The other tissues were marked as "others" in this thesis. These masks were

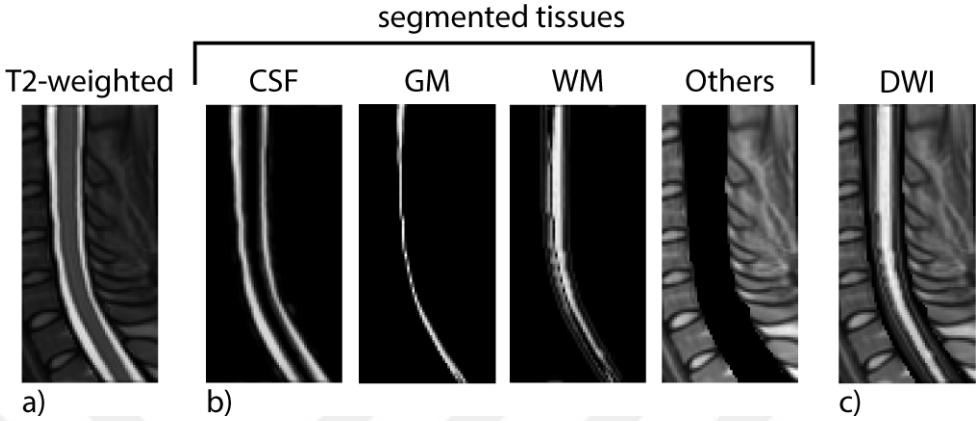

Figure 3.2: Process for simulating a diffusion-weighted image based on a T2-weighted input image. a) A sample T2-weighted sagittal image from PropSeg Spinal Cord Segmentation Toolbox. b) Segmented tissues: cerebrospinal fluid (CSF), gray matter (GM), white matter (WM) and "others". c) The resultant DWI image for $b = 500\,s/mm^2$ is depicted without any noise or phase added.

corrected using dilation/erosion operations, and spatially smooth transitions between tissues were achieved via frequency-domain apodization of the masks. The purpose of these corrections was to obtain simulated diffusion-weighted images that match the in vivo images, with soft transitions between tissue boundaries. The final tissue segmentations are displayed in Fig. 3.2b.

Next, a diffusion-weighted image was simulated based on the T2-weighted image. The mean ADC for GM and WM were taken as $900 \times 10^{-6}\,mm^2/s$, and $700 \times 10^{-6}\,mm^2/s$, respectively [4, 33]. The reported mean ADC values for CSF vary between $4600 \times 10^{-6}\,mm^2/s$ and $8000 \times 10^{-6}\,mm^2/s$ [4, 44]. Similarly, the in vivo experiments in this thesis yielded ADC values between $5500 \times 10^{-6} mm^2/s$ and $7500 \times 10^{-6}\,mm^2/s$ for CSF. Note that these ADC values for spinal CSF are biased by pulsation effects, as they are larger than free water diffusivity at body temperature. Here, we have chosen $7000 \times 10^{-6}\,mm^2/s$ for the ADC of CSF to match the in vivo diffusion-weighted images where CSF regions are devoid of signal. The tissues labeled as "others" were assumed to consist of muscle with an ADC of $1500 \times 10^{-6}\,mm^2/s$. To match the in vivo experiments, $b = 500\,s/mm^2$ was assumed. The resulting DWI image is shown in Fig. 3.2c.

Next, $NEX = 16$ acquisitions were simulated for the DWI image, each with zero initial phase. These acquisitions were then processed to induce similar k-space shift and phase errors as those observed in the in vivo experiments. Accordingly, a linear global-phase term was added in the image domain to model k-space shifts due to bulk motion during diffusion-sensitizing gradients. The k-space of each acquisition was shifted in k_x and k_y directions, with the amount of shift randomly picked from a uniform distribution between$(-0.2, 0.8)$ pixels. A two-dimensional local phase term was then added to each image to model the phase errors due to local motion dominant in the A/P direction. These local phases, $\phi(x, y)$, were added to locations near the nerve roots where the local motion was reported to be the most problematic [35] and were calculated as follows [5]:

$$\phi(x, y) = \gamma G \delta \Delta(x, y) \tag{3.8}$$

Here, x-direction is superior-inferior (S/I) direction, y-direction is the (A/P) direction, γ is the gyromagnetic ratio, G is the amplitude of the diffusion-sensitizing gradient (assumed to be in the A/P direction), δ is the duration of the diffusion-sensitizing gradient, and $\Delta(x, y)$ is the level of the motion in the A/P direction. Here, $\Delta(x, y)$ was modeled as a zero-mean unit-amplitude Gaussian window in the x-direction, and a Hanning-tapered window in the y-direction, affecting a region of size 36×16 pixels, i.e.,

$$\Delta(x, y) = \Delta_A W_{Gauss}(x) W_{Hanning}(y) \tag{3.9}$$

The standard deviation of the Gaussian window was randomly picked from a uniform distribution between $(0.7, 1.1)$ pixels for each acquisition, while the Hanning-tapered window was kept the same with a 4-pixel wide transition region on both sides and an 8-pixel wide flat region. The peak motion amplitude Δ_A was chosen from a uniform distribution between$(0.2, 0.4)$ mm, in accordance with the ones reported in the literature for the cervical spinal cord [34, 36]. Finally, complex-valued Gaussian noise was added to the k-space data of each acquisition at 13 different noise levels. The noise-to-signal ratio (NSR) of the images varied linearly between $(0, 0.750)$, where the standard deviation of noise was used to define the noise level (chosen to be identical for real and imaginary components)

and the peak image intensity was used to define the signal level. Equivalently, using $SNR = 1/SNR$, the SNR of each acquisition ranged between infinity and 1.33. To match in vivo experiments, a 62.5% k-space coverage was utilized for each acquisition (i.e., 37.5% of k-space data were replaced with zeros in k_y direction).

3.5 In vivo Experiments

In vivo DWI images of the cervical spinal cord of healthy subjects were acquired in the sagittal plane on a 3T GE MR 750 scanner, in accordance with the institutional review board protocol. Among the subjects imaged, two cases that demonstrated the signal cancellation issues were chosen prospectively. For the first subject, a 6-channel cervico-thoracic-lumbar (CTL) coil was used. To achieve high in-plane resolution, a reduced-FOV acquisition in the phase-encode (PE) direction was implemented via a 2D-selective RF excitation pulse [45]. ss-EPI readout with 192×48 imaging matrix and 62.5% partial k-space coverage in the PE direction was utilized. Diffusion weighting was applied in three orthogonal directions (S/I, A/P, R/L) with $b = 500\, s/mm^2$, a reasonable value for the spinal cord in low-SNR cases [32]. Other imaging parameters were:$0.94 \times 0.94\, mm^2$ in-plane resolution, FOV= $18 \times 4.5\, cm^2$, $4\, mm$ slice thickness, 6 slices,$TE = 51.3\, ms$, $TR = 3600\, ms$, NEX= 16 averages, and a total scan time of 3 min 52 sec. For the second subject, an 8-channel CTL coil was used. DTI images with 12 directions at $b = 500\, s/mm^2$ were acquired, along with two T2-weighted images. The imaging parameters were: $1 \times 1\, mm^2$ in-plane resolution,FOV= $20 \times 5\, cm^2$, $3\, mm$ slice thickness, 6 slices, $TE = 52\, ms, TR = 4600\, ms$, NEX= 16, and a total scan time of 17 min. Other imaging parameters were kept the same as in the first subject.

3.6 Alternative Reconstructions and Comparisons of Image Quality

Five alternative reconstructions were implemented for comparison. In common with the proposed reconstruction, all alternative reconstructions processed each of the multiple acquisitions with a refocusing reconstruction [22], followed by the POCS partial k-space reconstruction [41]. Each reconstruction then implemented a unique processing on outputs of the POCS algorithm:

1. Complex averaging (COMP): Multiple acquisitions were complex averaged.

2. NLM-filtered complex averaging: (NLM-COMP): Each acquisition was NLM filtered individually. The smoothing parameter was calculated immediately before filtering, as in the standard NLM filter [20]. As in PC-NLM, $d = 1$ and $M = 5$ were used. Finally, the NLM-filtered acquisitions were complex averaged.

3. Magnitude averaging (MAGN): Multiple acquisitions were magnitude averaged.

4. NLM-filtered magnitude averaging: (NLM-MAGN): The magnitude image of each acquisition was NLM filtered individually. The smoothing parameter was calculated immediately before filtering, based on the magnitude image. Again, $d = 1$ and $M = 5$ were used. Finally, the NLM-filtered acquisitions were magnitude averaged.

5. Model fitting (MOD-FIT): Magnitude images from multiple acquisitions were utilized to fit a Rician noise distribution model to each pixel [46]. Model fitting was performed via ML estimation using two independent variables of the Rice distribution, σ_g and η [47]. Here, σ_g is the standard deviation of the underlying complex Gaussian noise (identical for real and imaginary channels) and η is the true signal intensity for the diffusion-weighted image in the absence of noise. A typical strategy is to calculate σ_g from the background of an MRI image [48]. Due to lack of a background

region in reduced-FOV images, here the following is performed: First, an initial model fitting was performed for each pixel location individually, using the intensities from NEX= 16 repetitions. From the resulting map of σ_g values, the mean σ_g across all pixel locations was calculated. Finally, this mean σ_g value was enforced via a constrained model fit that only calculated η for each pixel. For pixels where a non-negative η cannot be fit, a small pixel intensity of $\sigma_g/100$ was assigned. Assuming that the underlying noise level is constant throughout the image, the intermediate step of calculating the mean σ_g significantly improves model fitting results, especially under high noise levels.

To assess the reconstructions in terms of image quality and the accuracy of the computed ADCs, a reference DWI image, DWI_{ref}, was produced without noise or phase errors. For unbiased comparison, a 62.5% k-space coverage was assumed for the reference image, processed with the refocusing reconstruction [22] and the POCS partial k-space reconstruction [41]. Reference ADC map, ADC_{ref}, was generated using DWI_{ref}. Comparisons were performed for two different scenarios: (1) when only global phase errors are present to test potential image deterioration when diffusion encoding is in non-problematic directions, and (2) when both global and local phase errors are present. To quantitatively assess image quality, the Peak-Signal-to-Noise (PSNR) metric was calculated:

$$PSNR = 10log_{10}\frac{MAX(DWI_{out})^2}{\frac{1}{|\Omega^2|}\sum\limits_{i\,\epsilon\,\Omega^2}\left[DWI_{ref}(x_i,y_i) - DWI_{out}(x_i,y_i)\right]^2} \tag{3.10}$$

where DWI_{out} is the output DWI image for a given method. To judge perceptual image quality, a secondary assessment was performed using the structural similarity (SSIM) index [49]. The built-in SSIM function of MATLAB 2016b (Mathworks, Natick, MA) was utilized with the default parameters of $C_1 = 1 \times 10^{-4}$ and $C_2 = 9 \times 10^{-4}$, where the dynamic range of the pixel intensities was between $(0, 0.25)$. For image quality assessments, Monte Carlo simulations were performed via repeating the simulations 10 times at 13 different noise levels ranging between NSR= 0 to NSR= 0.750. The PSNR and SSIM values were averaged across repeats. Note that image quality assessments were not performed for in

vivo datasets, since it was not possible to generate reference DWI images. Lastly, to analyze the noise statistics in different regions of the resulting images, a separate Monte Carlo simulation was performed with 40 repetitions at a noise level of NSR=0.25. For each repetition, the local and global phases were kept identical, and only the noise was randomly generated. For each method, the standard deviations across 40 repetitions were computed at each pixel location of the output DWI images.

3.7 DWI Simulation Results

Fig. 3.3 shows the magnitude and phase of each acquisition as well as the reconstructed images for all comparison techniques for the simulated dataset at NSR= 0.250 for two cases: (1) global phase only, (2) global and local phase issues. Accordingly, random local phase was added to two different locations along the length of the spinal cord (similar to the in vivo case illustrated in Fig. 2.5a. Images from the proposed and alternative reconstructions at three selected noise levels between NSR= $(0.125, 0.500)$ are given in Fig. 3.4, with identical gray-scale windowing. Here, NSR= 0.250 yielded DWI images that were visually the most similar to the in vivo results (see Fig. 3.3 for a closer look at results at this noise level for the cases with global phase only, and global and local phase errors).

In Fig. 3.4, regardless of the noise level, COMP that performs direct complex averaging results in signal cancellations. On the other hand, MAGN that performs magnitude averaging results in relatively poor SNR due to noise amplification, causing a washed-out appearance especially at higher noise levels. Although NLM-COMP and NLM-MAGN have visibly improved SNR due to filtering, NLM filtering on individual acquisitions does not address the signal cancellation or background noise amplification problems. MOD-FIT results in an unnatural look with a darkening of background at increasing noise levels, due to the difficulty of model fitting in low SNR regions. In contrast, the proposed reconstruction renders a combined image with visibly enhanced SNR without introducing signal cancellations.

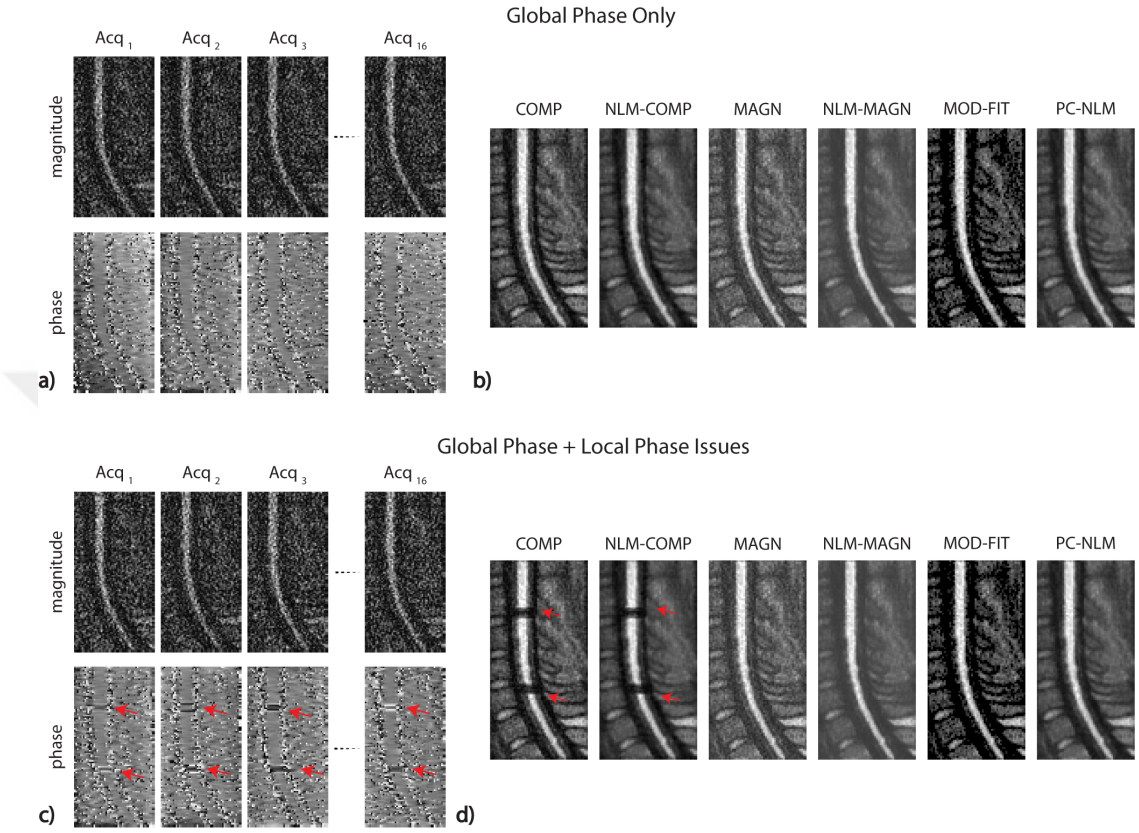

Figure 3.3: DWI simulation results at NSR=0.250 for the case of global phase only and the case of both global and local phase errors. a) Magnitude and phase of each of the acquisitions for the simulated data without any local phase errors, displayed following a global phase correction and a partial k-space reconstruction. b) Results of alternative reconstructions and the proposed method are depicted. Note the suppressed noise in the proposed reconstruction when compared to MAGN and NLM-MAGN. Since there are no local phase errors, COMP and NLM-COMP do not show any signal cancellations. NLM-COMP improves image SNR when compared to COMP. MOD-FIT results in an unnatural look, especially in low signal intensity regions. The proposed method has comparable image quality to that of NLM-COMP. c) Magnitude and phase of each of the acquisitions for the simulated data with both global and local phase errors, displayed following a global phase correction and partial k-space reconstruction. Phase errors, shown by red arrows, are added to the DWI images with the diffusion-encoding along the A/P direction. d) Results of alternative reconstructions and the proposed method are depicted. Signal cancellations due to phase errors are prominent in both COMP and NLM-COMP. Likewise, high-level noise causes noise accumulation in MAGN and the preceding NLM filter is not sufficient to overcome this issue in NLM-MAGN. The performance of MOD-FIT is almost unchanged, with a darkening in the background regions. On the other hand, the proposed PC-NLM renders a solution without any phase cancellations while suppressing noise.

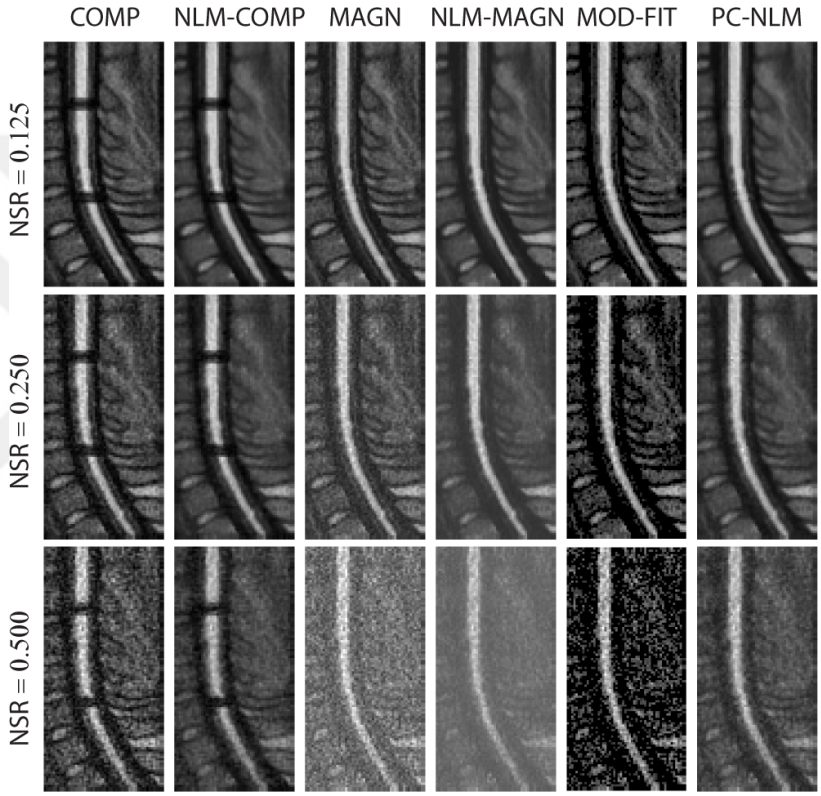

Figure 3.4: DWI simulation results at three different NSR levels (0.125, 0.250, and 0.500). Reconstruction outputs of the proposed method and alternative methods are displayed for NEX = 16. COMP and NLM-COMP show signal cancellations due to phase errors regardless of the noise level. On the other hand, MAGN and NLM-MAGN yields pixel intensities that are comparable to the noise floor, especially at higher noise levels. MOD-FIT is sensitive to noise and yields an unnatural look as the noise level increases. The proposed reconstruction achieves superior noise suppression compared to methods based on magnitude averaging and model fitting, and alleviates signal cancellations compared to methods based on complex averaging.

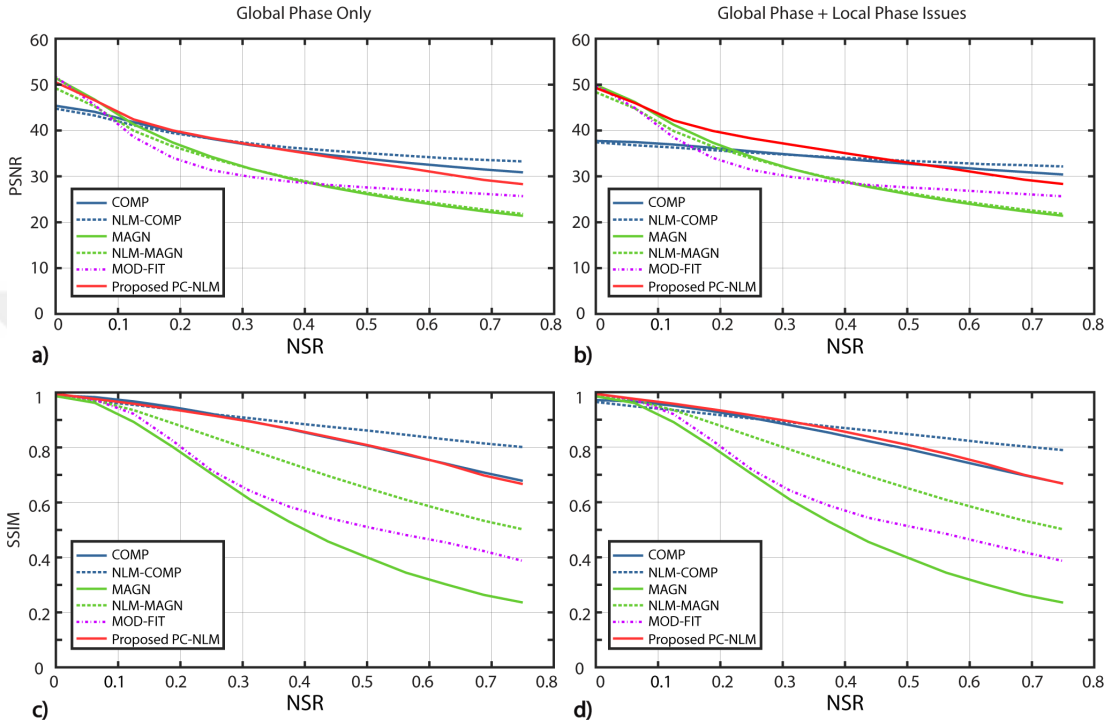

Figure 3.5: Image quality assessment for the proposed and alternative reconstructions based on PSNR and SSIM metrics. The proposed reconstruction achieves a high level of image quality across a broad range of realistic noise levels (NSR < 0.400). a) In the presence of only global phase errors, PSNR values for COMP and NLM-COMP remain at high levels for all NSR values. Meanwhile, PSNR for MAGN, NLM-MAGN, and MOD-FIT drop immediately with increasing noise. b) When local phase errors are also incorporated, PSNR for COMP and NLM-COMP decrease approximately $1 - 7\,dB$ due to local signal cancellations. The trends in MAGN, NLM-MAGN, and MOD-FIT remain the same. The proposed reconstruction shows PSNR values that converge MAGN at low noise levels and that converge COMP at high noise levels around NSR ≈ 0.500. This result suggests that PC-NLM captures the phase robustness of MAGN and noise robustness of COMP simultaneously. c, d) SSIM values of COMP and NLM-COMP do not change significantly between the two scenarios (i.e., global phase errors vs. both global and local phase errors). Thus, SSIM is not sufficiently sensitive to capture phase-induced signal cancellation. SSIMs for MAGN and NLM-MAGN drop significantly with increasing NSR due to noise accumulation. SSIM for MOD-FIT drops similarly at higher NSR due to noise sensitivity. Lastly, the proposed reconstruction maintains the highest SSIM values for $NSR < 0.300$, and comparable SSIM to COMP at higher noise levels.

Image quality with the proposed and alternative reconstructions was assessed via the PSNR metric. The simulations were repeated 10 times at 13 different noise levels between NSR= $(0, 0.750)$, and the PSNR values were averaged across repeats. Fig. 3.5a shows the PSNR values in the presence of global phase errors only. PSNR values for COMP and NLM-COMP are in $30 - 45\,dB$ range at all noise levels, and higher than PSNR values for MAGN, NLM-MAGN, and MOD-FIT when NSR>0.150. (Note that MOD-FIT shows degradation in image quality starting as early as NSR>0.100.) This trend is expected, as robustness against noise amplification is the main advantage of complex averaging. Meanwhile, there are some subtle differences in quality introduced by NLM filtering for complex averaging and magnitude reconstructions (i.e., between NLM-COMP and COMP, and between NLM-MAGN and MAGN). While NLM filtering slightly reduces PSNR at relatively low noise levels, it yields a minor increase in PSNR at higher noise levels. These results suggest that NLM causes smoothing of detailed image features to suppress noise, and thus its advantages are more apparent at higher noise levels. The proposed reconstruction maintains a favorable trade-off between NLM-COMP and NLM-MAGN at very low and high noise levels (NSR < 0.1 and NSR > 0.4), and superior performance compared to all other techniques in a broad range of realistic noise levels ($0.1 <$ NSR < 0.4). At NSR= 0.250, the proposed method has comparable PSNR to COMP (38.3 dB vs. 38.2 dB), 4 dB higher PSNR than MAGN (38.3 dB vs. 34.3 dB), and 6.9 dB higher PSNR than MOD-FIT (38.3 dB vs. 31.4 dB). Fig 3.5b shows the PSNR values in the presence of both global and local phase errors. Compared to the simulations with only global phase errors, PSNR values drop approximately $1.0 - 7.0dB$ for COMP and NLM-COMP due to local signal cancellations. Meanwhile, PSNR values for MAGN, NLM-MAGN, and MOD-FIT are not affected. Still, MAGN and MOD-FIT yield better PSNR performance at low noise levels, and COMP yields better PSNR performance at high noise levels. Note that the proposed technique achieves PSNR similar to MAGN at low noise and COMP at high noise, capturing the phase robustness of MAGN and noise robustness of COMP simultaneously. When compared to Fig. 3.5a, the PSNR values of the proposed PC-NLM method are only reduced by $0.5 - 1.0\,dB$ for NSR<0.100, and this difference reduces to less than $0.1\,dB$ at higher noise levels. At NSR= 0.250, the proposed method

has 2.8 dB higher PSNR than COMP (38.3 dB vs. 35.5 dB), 4 dB higher PSNR than MAGN (38.3 dB vs. 34.3 dB) and 6.9 dB higher PSNR than MOD-FIT (38.3 dB and 31.4 dB). At a higher noise level of NSR= 0.500, PC-NLM has 6.6 dB higher PSNR than NLM-MAGN (33.0 dB vs. 26.4 dB), 5.4 dB higher than MOD-FIT (33.0 dB vs. 27.6 dB), and comparable PSNR to NLM-COMP (33.0 dB vs. 33.4 dB). It is important to note that although COMP and NLM-COMP yield the highest PSNR at high noise levels, they both suffer from signal cancellation. An aggregate PSNR metric over the entire image can be ineffective in capturing these local artifacts. To assess the perceptual quality of DWI images that also reflect image sharpness, a secondary assessment was performed using the SSIM metric. Fig. 3.5c and 3.5d show the SSIM values in the presence of only global phase errors and in the presence of both global and local phase errors, respectively. Overall, SSIM values for all reconstruction methods tested remain similar between the two scenarios depicted in Figs. 3.5c and 3.5d. SSIM values for COMP and NLM-COMP are higher than those for MAGN, NLM-MAGN, and MOD-FIT when NSR$>$ 0.100. Compared to PSNR, the quality improvement with NLM filtering at high noise levels is more clearly captured in SSIM measurements. For instance, SSIM for MAGN drop from 0.99 to 0.24 as the noise level is increased, whereas SSIM for NLM-MAGN only drops from 0.99 to 0.51 in the same range. The SSIM for MOD-FIT also drops significantly from 0.99 to 0.34 at increasing noise levels. Lastly, the proposed reconstruction maintains the highest SSIM values for NSR$<$0.300, and comparable SSIM to COMP at higher noise levels. Again, it should be noted that both COMP and NLM-COMP suffer from signal cancellations despite their high SSIM performances. Similar to PSNR, SSIM is an aggregate metric across the entire image that is insufficiently sensitive in detecting local artifacts. For the simulated datasets, ADC maps were also compared with ADC_{ref}. Fig 3.6 shows the mean ADC values in three different regions of interest (ROIs), selected as follows:

1. A region with no phase issues and relatively high SNR (due to high local coil sensitivities),

2. A region with local phase issues,

3. A region with local phase issues and relatively low SNR (due to low local coil sensitivities).

The plots in Fig. 3.6 show the average ADC values within each ROI across 10 Monte Carlo simulations.

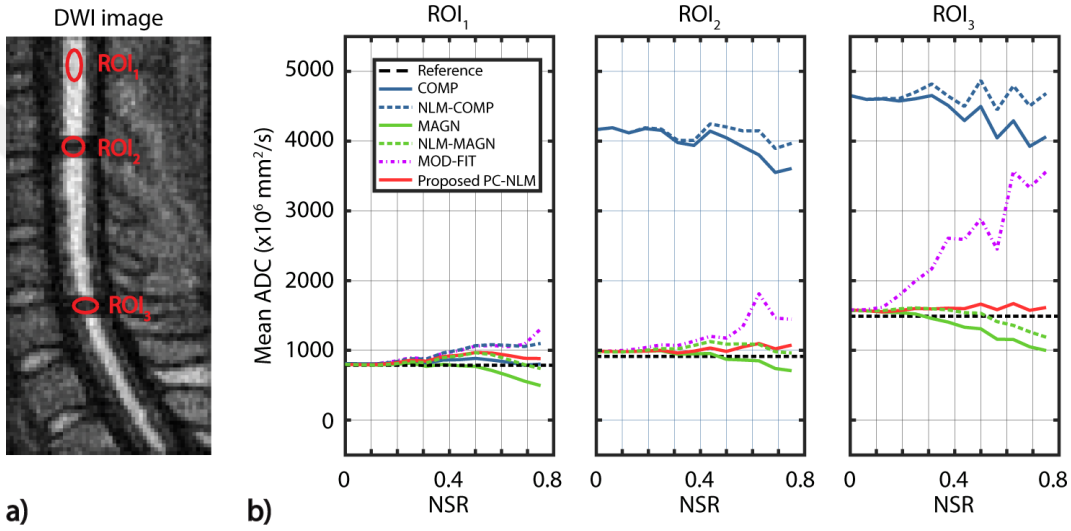

Figure 3.6: Comparison of ADC values with respect to the reference ADC map. a) Three ROIs are selected to analyze the effects of noise accumulation and phase-related signal cancellations. ROI_2 and ROI_3 have phase issues, while ROI_1 does not. ROI_3 also has reduced SNR. b) COMP and NLM-COMP yield overestimated results in ROI_1 as noise increases. Signal cancellations in COMP and NLM-COMP lead to overestimation of the ADCs in ROI_2 and ROI_3, while noise accumulation in MAGN and NLM-MAGN result in underestimation of the ADCs especially in ROI_3. MOD-FIT overestimates the ADC values at higher noise levels, especially in ROI_2 and ROI_3. The proposed reconstruction is robust against noise in the ADC estimations in all three ROIs.

With respect to ADC_{ref} in ROI_1, COMP, NLM-COMP, MOD-FIT, and the proposed reconstruction tend to slightly overestimate the ADC as noise increases. MAGN, on the other hand, underestimates the ADC at high noise levels due to noise amplification. NLM-MAGN also displays a similar trend, but only at very high noise levels. In ROI_2 and ROI_3, signal cancellations in COMP and NLM-COMP lead to significant overestimation of ADC values, while noise amplification in MAGN and NLM-MAGN result in underestimation of ADC especially in ROI_3. MOD-FIT overestimates the ADC values even at realistic noise levels around NSR$= 0.250$, especially in ROI_3. This problem quickly escalates at higher

	Global Phase Only			Global+Local Phase Issues		
	ROI_1	ROI_2	ROI_3	ROI_1	ROI_2	ROI_3
COMP	0.0578	0.0605	0.0576	0.0585	0.0469	0.0401
NLM-COMP	0.0454	0.0477	0.0466	0.0452	0.0446	0.0387
MAGN	0.0581	0.0606	0.0573	0.0591	0.0558	0.0521
NLM-MAGN	0.0452	0.0488	0.0462	0.0460	0.0446	0.0408
MOD-FIT	0.0603	0.0629	0.0690	0.0613	0.0583	0.0615
PC-NLM	0.0306	0.0321	0.0342	0.0314	0.525	0.0485

Table 3.1: Noise statistics in three different ROIs. The numbers report the normalized noise levels (i.e., average of the noise std over each ROI, normalized by the highest pixel intensity in the reference DWI image).

noise levels due to the difficulty of model fitting in low-SNR cases. The proposed reconstruction yields ADC values that closely match the reference ADCs in all three ROIs, with a relatively minor tendency to overestimate. It is important to note that while the error in the ADC is overall comparable for the proposed method and MAGN/NLM-MAGN, the proposed method achieves superior noise suppression and significantly higher PSNR/SSIM results when compared to those two methods. Lastly, the noise statistics were analyzed via a Monte Carlo simulation with 40 repetitions at NSR= 0.250. Global and local phases were kept identical among repetitions to investigate their effects on local noise characteristics. Fig. 3.7 shows the standard deviation (std) of pixel intensities across 40 repetitions for each reconstruction technique (see Table 3.1 for values in three different ROIs).

COMP shows high std throughout the spinal cord, except for regions of local signal cancellations where std is lower due to lower pixel intensities. MAGN shows uniform std throughout the spinal cord, with std levels matching that of COMP except in areas of local signal cancellations. As expected, NLM-COMP and NLM-MAGN have relatively lower std than their non-filtered counterparts. Furthermore, NLM filtering yields spatially varying noise based on the signal level. MOD-FIT results in the highest std across all techniques, suffering especially in the background regions with lower signal intensities. In contrast, the proposed

PC-NLM yields the lowest std in regions without local signal cancellations. Even in cancellation regions, the std for PC-NLM does not exceed that of MAGN. This can be attributed to the fact that, in the presence of excessive local phase variations, PC-NLM cannot find a similar patch in other NEXs and thus leaves the central pixel unaveraged. Since filtered NEXs are then magnitude averaged, the noise characteristics would then match that of MAGN in this worst case. For noise statistics in the presence of global phase only, see Fig. 3.7 and Table 3.1.

3.8 In vivo Experiment Results

Figure 3.8a and 3.8b display the results in the first subject, for single-channel and combined-channel DWI images with diffusion-weighting in the (A/P) direction. The red arrows indicate regions of signal cancellation in COMP and NLM-COMP reconstructions. The blue arrows indicate regions of noise amplification in MAGN, NLM-MAGN, and MOD-FIT reconstructions, prominent in the inferior parts of the spinal cord due to reduced local coil sensitivity. In contrast, the proposed reconstruction suppresses signal cancellations and noise amplification, and ensures superior depiction of the spinal cord even in the inferior regions. As a trade-off of noise suppression, there is a slight loss of resolution in NLM-COMP, NLM-MAGN, and PC-NLM (e.g., visible in the cerebellum region in Fig. 3.8). This effect is less pronounced for the proposed method, thanks to the automated tuning of the smoothing parameter. The mean ADC values in the spinal cord were analyzed by selecting three different ROIs (see Fig. 3.8c):

1. A region with no phase issues and relatively high SNR,
2. A region with local phase issues,
3. A region with relatively low SNR, but no visible phase issues.

Figure 3.8d shows the ADC maps generated by each method, and Table 3.2 lists the mean and standard deviation of ADC values in each ROI and in each ADC map.

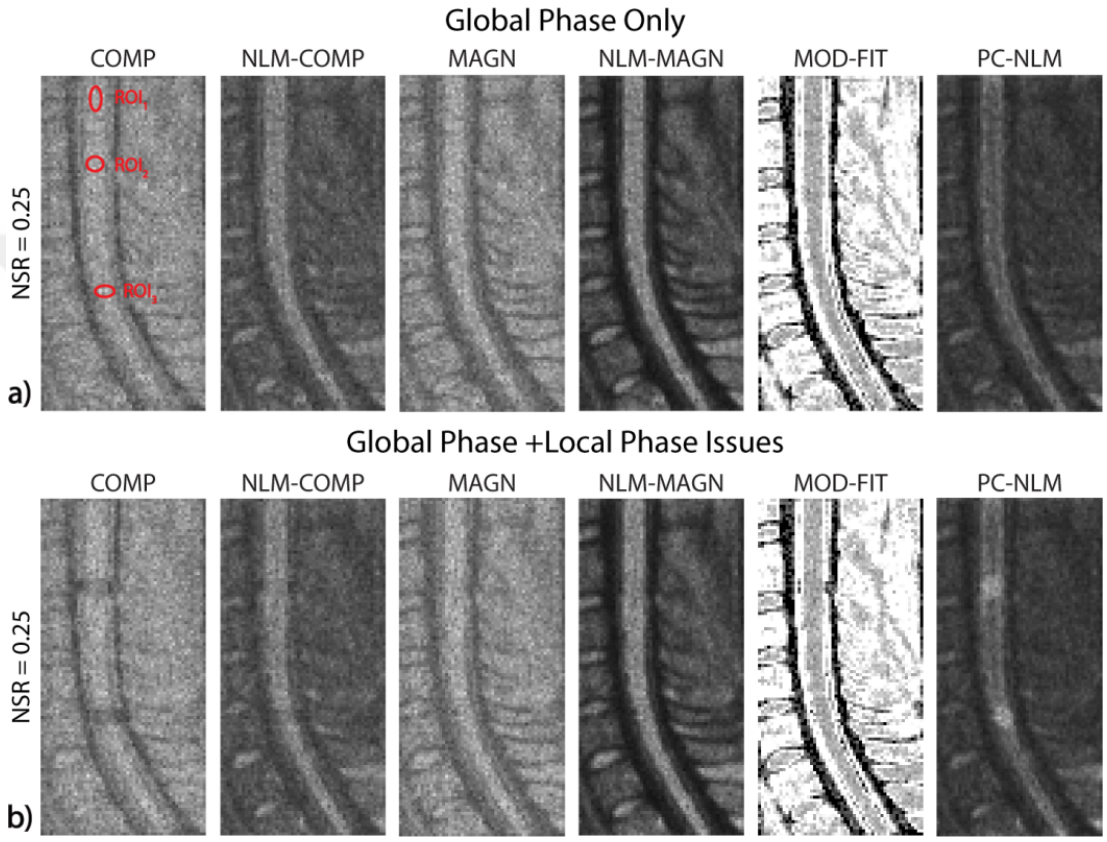

Figure 3.7: Local noise statistics for all reconstruction techniques at NSR=0.250, for the case of global phase only and the case of both global and local phase errors. a) For global-phase-only case, COMP and MAGN result in comparable high std. MOD-FIT has the highest standard deviation among all reconstruction techniques, due to its noise sensitivity. NLM-COMP and NLM-MAGN have relatively reduced std when compared to their non-filtered counterparts. PC-NLM yields the lowest std, demonstrating robustness against noise. b) For the case of both global and local phase errors, the noise statistics are almost unchanged for MAGN, NLM-MAGN, and MOD-FIT, as expected. In regions of signal cancellations, std for COMP and NLM-COMP are reduced due to lower pixel intensities in those regions. PC-NLM yields the lowest std in regions without signal cancellations. In cancellation regions, std of PC-NLM is slightly lower than that of MAGN. The noise statistics in three different ROIs (marked over the COMP image in (a)) are listed in Table 3.1.

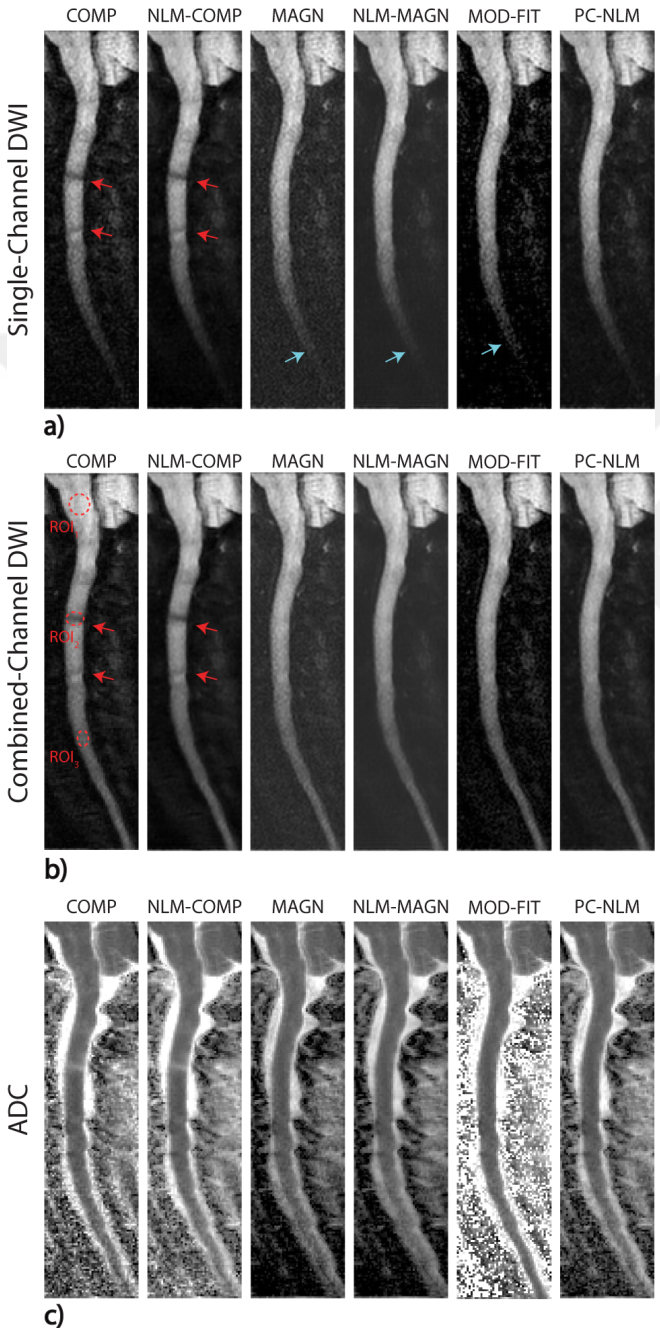

Figure 3.8: Results for in vivo DWI of the spinal cord for the first subject. Images with diffusion-encoding along the A/P direction are displayed. a) Reconstructions of single-channel images. Local signal cancellations due to phase errors are prominent in COMP and NLM-COMP (red arrows). MAGN, NLM-MAGN, and MOD-FIT overcome signal cancellations, but noise accrual or noise sensitivity occurs (blue arrows). b) Reconstructions of combined-channel images. Signal cancellations (red arrows) are still present in COMP and NLM-COMP. Although combining across channels improves depiction of the inferior parts of the spinal cord, noise amplification remains a problem in MAGN and NLM-MAGN. While MOD-FIT also benefits from combining across channels, the unnatural darkening in the background persists. In contrast, the proposed reconstruction suppresses signal cancellations and noise amplifications. For the quantitative analyses of the mean ADC values, three different ROIs were selected, as marked on the DWI image from COMP. c) ADC maps for all reconstructions. The mean ADC values in the selected ROIs are listed in Table 3.2.

	ROI_1	ROI_2	ROI_3
COMP	696 ± 191	1549 ± 432	742 ± 240
NLM-COMP	699 ± 160	1557 ± 420	841 ± 223
MAGN	668 ± 189	549 ± 255	613 ± 243
NLM-MAGN	671 ± 165	558 ± 233	739 ± 228
MOD-FIT	720 ± 196	633 ± 273	864 ± 265
PC-NLM	687 ± 170	570 ± 247	729 ± 233

Table 3.2: Mean and standard deviation of Apparent Diffusion Coefficient (ADC) values [$\times 10^{-6}\, mm^2/s$]. Signal cancellations in COMP and NLM-COMP result in overestimation of the ADC values, whereas noise accumulation in MAGN and NLM-MAGN leads to underestimation of the ADC values. MOD-FIT also overestimates ADC values, especially in ROI_3 where the SNR is low. The proposed PC-NLM reconstruction prevents signal cancellations while preserving the accuracy of the ADC estimates.

The in vivo results listed in Table 3.1 are consistent with the trends in Fig. 3.6 for the simulated DWI images. For example, in ROI_1 where there are no phase issues, COMP is expected to provide the most accurate results. For that region, the proposed method yields ADC values that closely match those of COMP, while MAGN and NLM-MAGN underestimate and MOD-FIT overestimates the ADC values, as expected. In ROI_2 where there are visible phase issues, COMP and NLM-COMP yield unreasonably high ADC values. Comparing these results to the simulation results in Fig. 3.6b, one can presume that the true ADC is somewhere in between the results of MAGN and PC-NLM. Hence, it can be deduced that MOD-FIT overestimates the ADC values for this ROI. In ROI_3 where SNR is low but there are no visible phase issues, COMP, NLM-MAGN, and PC-NLM yield similar ADC values. MOD-FIT and NLM-COMP give higher ADC values, while MAGN yields lower ADC values, as predicted by high-NSR cases in ROI_1 of Fig. 3.6b. Importantly, the proposed method preserves the accuracy of the ADC maps while improving image quality, despite the presence of significant local phase errors in the acquisitions.

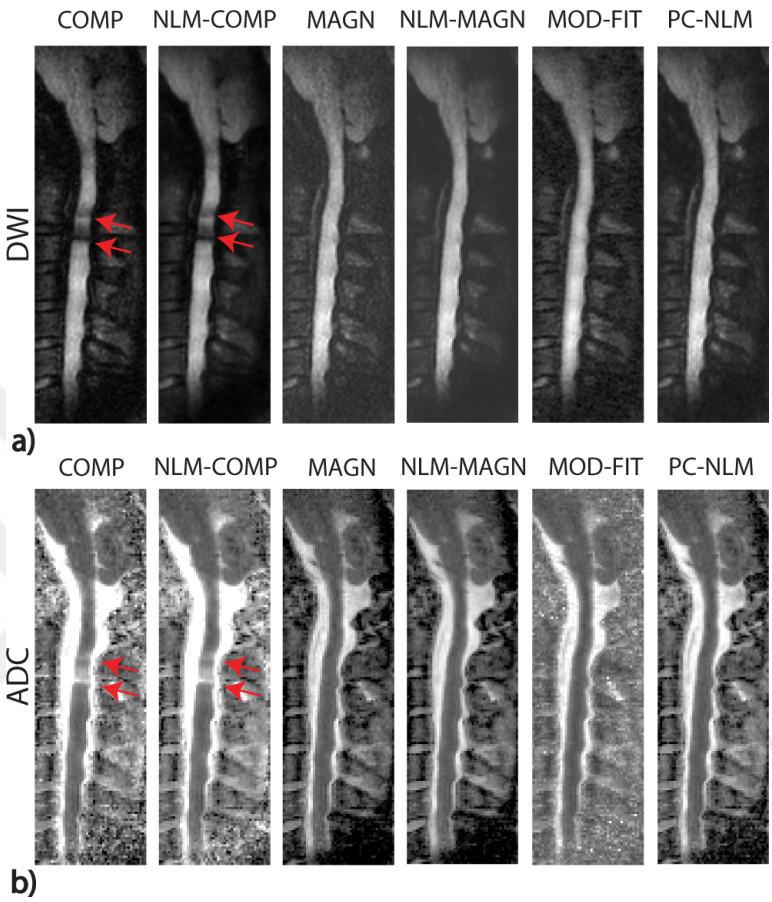

Figure 3.9: Reconstructions from in vivo DTI acquisitions of the spinal cord for the second subject. Images with diffusion-encoding along the A/P direction are displayed. a) DWI images are shown for the proposed PC-NLM and alternative reconstructions. Note the suppressed noise level and the lack of signal cancellations with the proposed reconstruction. b) The corresponding ADC maps.

Figure 3.9 shows the results for the second subject, where DWI images and ADC maps are displayed for the case when diffusion-weighting was in the A/P direction. Once again, COMP and NLM-COMP reconstructions suffer from clearly visible signal cancellation (red arrows) near the discs, which in turn correspond to locations where nerve roots exit the cord. The noise accumulation problem in MAGN and NLM-MAGN is especially prominent near the pons and in the inferior regions of the cervical spine. While the results for MOD-FIT and PC-NLM match visually for the DWI image, the ADC map for MOD-FIT reveals overestimation problems in regions of low signal intensity. The proposed PC-NLM

reconstruction provides visually improved image quality that is devoid of signal cancellations in these regions, with high fidelity ADC maps.

To show the effects of number of acquisitions on the filter performance, the proposed PC-NLM and all of the alternative comparison techniques are reconstructed for NEX= 8 and NEX= 4 cases in Fig. 3.10. When the in vivo data from the first subject is reconstructed for NEX= 8 or NEX= 4 (i.e., using only a subset of the 16 acquisitions), COMP and NLM-COMP result in more severe local signal cancellations. In addition to that, SNR of MAGN and NLM-MAGN drop significantly, and the performance of MOD-FIT severely deteriorates as NEX decreases. The proposed PC-NLM, though, asserts a robust performance and superior image quality over all the alternative comparison techniques without any local signal cancellation issues.

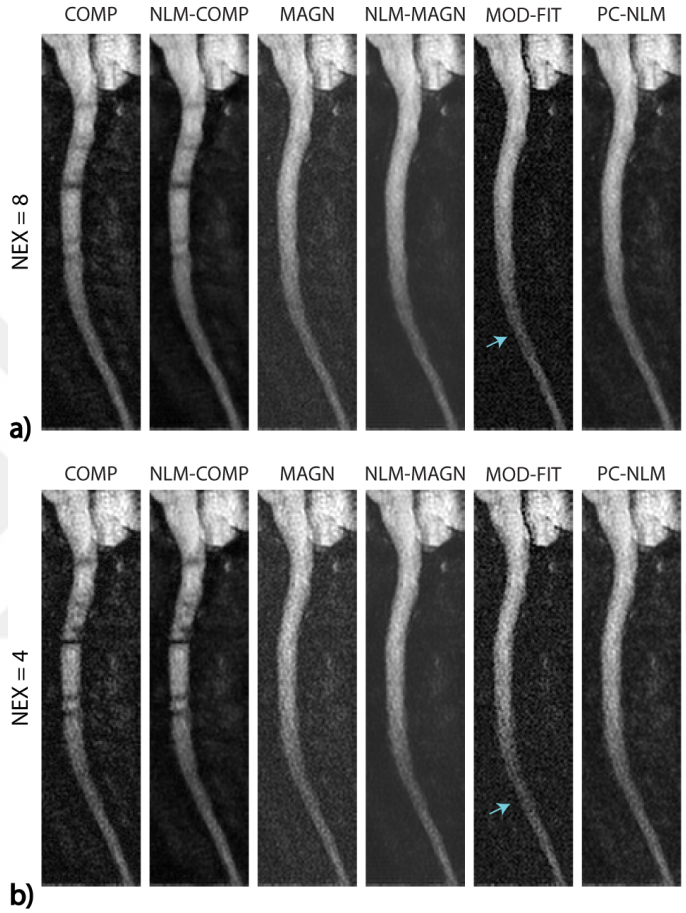

Figure 3.10: Results for in vivo DWI of the spinal cord for the first subject, for a) NEX=8 and b) NEX=4 (i.e., using only a subset of the 16 acquisitions). As NEX is reduced, the image qualities for COMP, NLM-COMP, and MOD-FIT significantly deteriorate. The number and extent of signal cancellation regions are increased for COMP and NLM-COMP, as the likelihood of having a NEX with similar phase is reduced when there are fewer NEXs. The image quality for MOD-FIT especially suffers in inferior parts of the spine (shown by blue arrows) due to reduced coil sensitivities. This problem is further exacerbated as NEX is reduced, as model fitting becomes more challenging when there are fewer samples for a low-SNR pixel. MAGN, NLM-MAGN, and PC-NLM show lower SNR with reduced NEX, but the image qualities are not affected otherwise. Overall, when compared to the other reconstruction techniques, PC-NLM has visibly improved image quality at both NEX=8 and NEX=4, and it does not suffer from local signal cancellations or noise accumulation problems.

Chapter 4

Phase-Correcting Non-Local Means Filtering for DTI

This chapter is based on the publication titled 'Kafali SG, Cukur T, Saritas EU. Joint Non-local Means Reconstruction for Correction of Phase-Induced Errors in Diffusion Tensor Imaging'. In Proceedings of the 25th Annual Meeting of ISMRM, Hawaii, USA, 2017. p.3332.

4.1 Modifications to PC-NLM for DTI

For DTI applications, the PC-NLM filter is modified to incorporate the joint information from different diffusion-weighting directions. The overall image reconstruction scheme is summarized in Fig. 4.1. Global phase of each diffusion-weighted image was corrected via refocusing reconstruction [22], followed by a POCS partial k-space reconstruction [41], same as in the PC-NLM for DWI case. The resultant images were then processed with a modified version of the PC-NLM filter, named "joint PC-NLM" in this thesis.

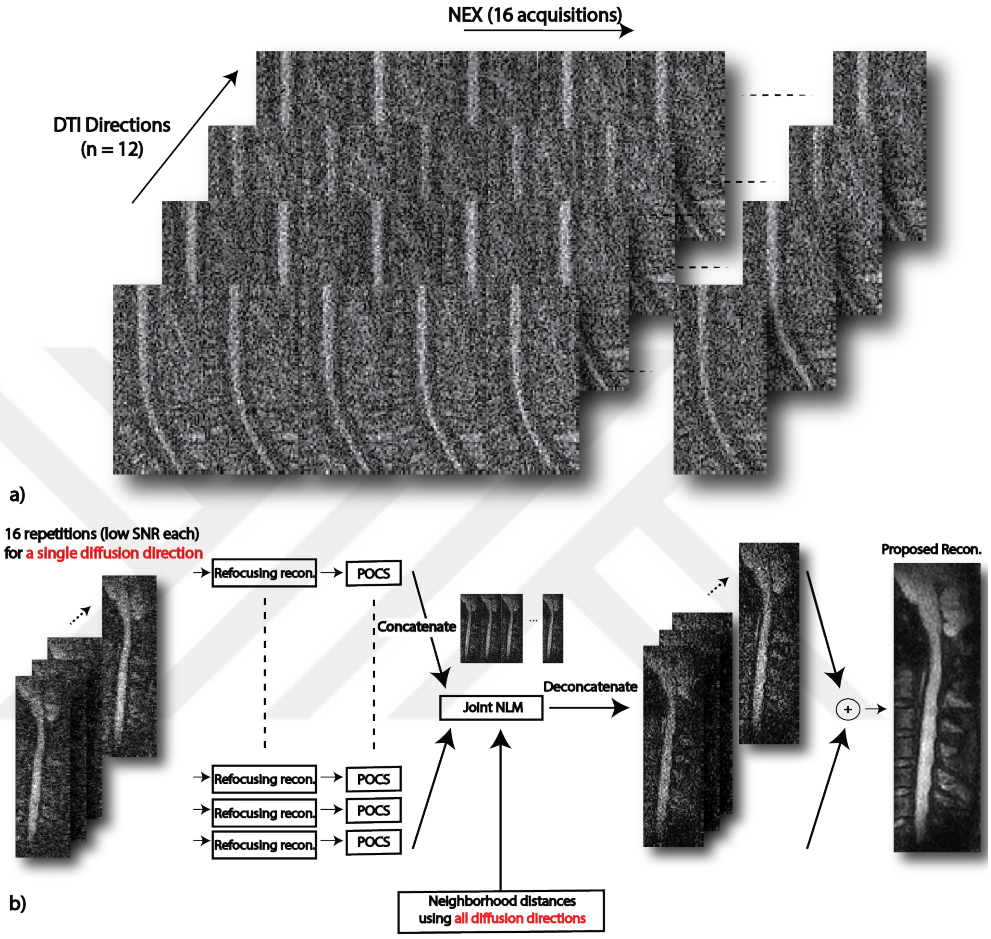

Figure 4.1: a) Multiple acquisitions of each diffusion direction are concatenated in 2D, and all diffusion directions are concatenated in 3D, forming a large volumetric image. This 3D volumetric image is used for calculating neighborhood similarities, quantified by the Euclidian distance between neighborhoods. Here the DTI images are shown for simulated data. b) Each acquisition of each diffusion direction is phase corrected individually with refocusing reconstruction. POCS algorithm is applied to reconstruct the k-space from partially sampled data. Then the complex-valued acquisitions are concatenated in 2D. To set the amount of blurring, the smoothing paramater is calculated considering all diffusion directions. Resulting images are processed with the joint PC-NLM algorithm, then deconcatenated and magnitude averaged.. This entire procedure is repeated for each direction, using the joint Euclidian distance calculated in part (a). Here, the results are shown for a single direction of the in vivo dataset.

Accordingly, all complex-valued NEXs were concatenated in 2D. The images from different diffusion-encoding directions were then concatenated along the third dimension. The joint PC-NLM filter searched for similar neighborhoods, in the resultant 3D matrix, shown in Fig. 4.1a.

For a given diffusion direction z, the pixel intensity after filtering was determined by averaging central pixels of similar neighborhoods:

$$m_{NLM}(x_i, y_i, z) = \sum_j w(x_i, y_i; x_j, y_j) m(x_j, y_j) \tag{4.1}$$

To find the weight $w(x_i, y_i; x_j, y_j)$, for each diffusion direction z, the joint Euclidean distance between the neighborhoods were calculated by considering *all* diffusion-encoding directions. This important step helps preserve the integrity of the FA map.

$$w(x_i, y_i; x_j, y_j) = \frac{1}{Z_i} e^{-\frac{|m(N(x_i, y_i, :)) - m(N(x_j, y_j, :))|^2}{h^2}} \tag{4.2}$$

Here, ":" denotes selection of all diffusion-encoding directions in the 3D volumetric matrix. Hence, the neighborhood similarity is computed via a Euclidian distance based on the similarity of images from all diffusion directions. Z_i is a normalization constant, ensuring that the filter weights sum up to 1, i.e.,

$$\sum_j w(x_i, y_i; x_j, y_j) = 1 \tag{4.3}$$

The smoothing parameter h is determined by the following equation considering all the diffusion directions:

$$h^2 = 2\beta \ |N_i| \sum_{k=1}^{N_{diff}} {\sigma_k}^2 \tag{4.4}$$

Here, N_{diff} is the total number of diffusion directions. Note that the smoothing parameter, h, is identical for all diffusion directions. The standard deviations σ_k were computed directly from the images for each diffusion direction using Eqn. 3.5, and β was set to 0.5 to set the trade-off between SNR and resolution [20]. This

entire procedure was repeated for each direction, using the same joint Euclidian distance, and hence the same weights. Utilizing the same smoothing parameter and the same weights for each direction ensures consistent processing of images from all directions.

4.2 DTI Simulations

For quantitative assessment, a simulated DTI set for spinal cord was generated using PropSeg segmentation toolbox for 12 directions [42, 43]. All the imaging parameters such as b value, TE, TR, FOV, NEX and in-plane resolution were kept identical as in the PC-NLM for DWI case. The DTI data was simulated to incorporate the same issues as in the DWI case, i.e., the same problems such as complex Gaussian noise (with NSR = 0.250), local motion, global phase errors were added to each of the multiple acquisitions. The amount of k-space shifts and global phase were also identical with the PC-NLM for the DWI case. As the local motion along spinal cord is dominant along the A/P direction, the local phase issues were added only in this direction [5, 34, 36].

4.3 In vivo Experiments

In vivo DTI images of the cervical spinal cord of healthy subjects were acquired in the sagittal plane on a 3T GE MR 750 scanner, in accordance with the institutional review board protocol. Among the subjects imaged, one case demonstrating the signal cancellation issues was chosen prospectively. This dataset was the same as the one from the second subject of the DWI in vivo experiments in Chapter 3. Different from the DWI case, all of the diffusion directions are considered for DTI analyses. As explained in Chapter 3.4 In Vivo Experiments, an 8-channel CTL coil was used with a reduced-FOV acquisition in the phase-encode (PE) direction implementation via a 2D-selective RF excitation pulse [45]. ss-EPI readout with 192×48 imaging matrix and 62.5% partial k-space coverage in the

PE direction was utilized. DTI images with 12 directions at $b = 500\,s/mm^2$ were acquired, along with two T2-weighted images. The imaging parameters were: $1 \times 1\,mm^2$ in-plane resolution, FOV= $20 \times 5\,cm^2$, $3\,mm$ slice thickness, 6 slices, $TE = 52\,ms, TR = 4600\,ms$, NEX= 16, and a total scan time of 17 min.

4.4 Alternative Reconstructions and Quantitative Comparison Techniques

For comparison, two additional image reconstructions were implemented. For both cases, refocusing reconstruction and partial k-space reconstruction were first performed, as in the proposed reconstruction. Then, (1) the magnitude average (MAGN) and (2) complex average (COMP) of NEXs were computed. For a quantitative assessment, the Euclidean distance between the principle eigenvectors of the reference data and each method were computed. To assess the reconstructions in terms of the accuracy of the estimated FA maps, reference gray-scale and color FA maps were produced without noise or phase errors.

4.5 DTI Simulation Results

DTI simulation results with reference (ground-truth) images are displayed in Fig. 4.2 for isotropic DWI, gray-scale, and color-coded FA maps. The main drawback of COMP is the signal cancellations, although this approach benefits from higher SNR. The local signal cancellations result in inaccurate estimation of the main diffusion direction. MAGN on the other hand, does not suffer from local signal cancellations. The corresponding FA maps are not affected by the local phase issues, yet the SNR is lower due to noise accumulation, which can be seen especially at the background in both FA maps. The proposed joint PC-NLM supresses the background noise without local signal cancellations.

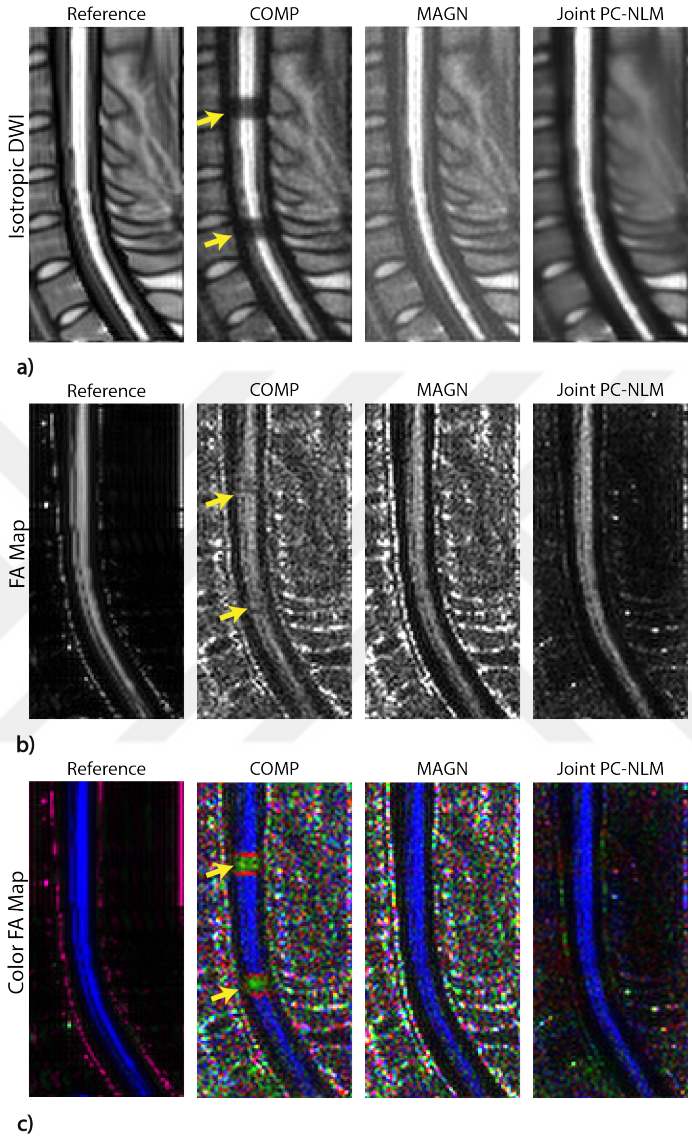

Figure 4.2: Simulation results in cervical spinal cord DTI. For image quality assessment, reference (ground-truth) images are also given for a) isotropic DWI b) grayscale FA maps, and c) color-coded FA maps. MAGN is degraded by noise accumulation in the background, whereas COMP leads to incorrect principle diffusion directions (yellow arrows). The proposed joint PC-NLM provides the closest match to the reference images, overcoming the local phase problems while reducing the noise in the background of the FA maps.

Again, the proposed reconstruction overcomes the local phase problems while reducing the noise in the background of the FA maps. The histograms of these

differences are shown in Fig. 4.4 and 4.3. Grayscale FA error is measured as the absolute difference between the reference FA value and the corresponding reconstruction technique, whereas the color-coded FA error is calculated as the Euclidean distance between the principle eigenvector in the color FA map of the reference and the corresponding reconstruction technique. These metrics were computed only for the segmented white matter and gray matter regions and their vicinity. Both Fig. 4.4 and 4.3 show that the proposed joint PC-NLM technique yield the smallest mean and median estimation errors in terms of grayscale and color-coded FA values.

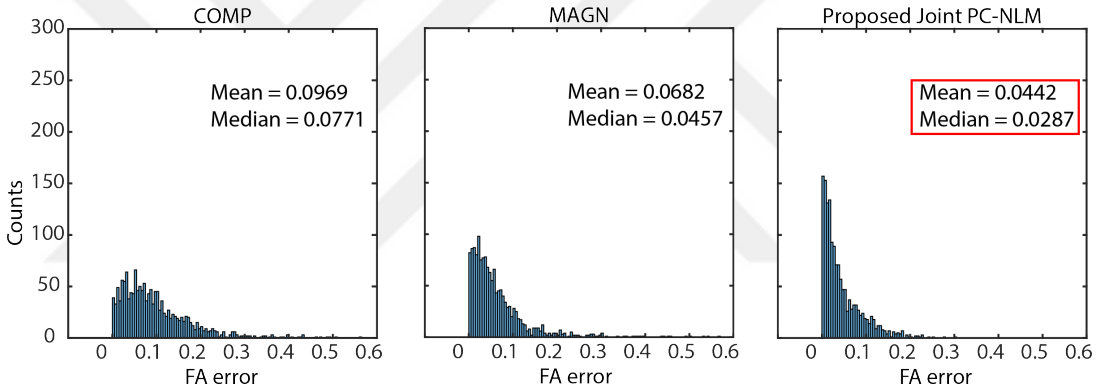

Figure 4.3: Histograms of the grayscale FA errors (with respect to the reference simulated data). The grayscale FA error is calculated as the absolute difference between the reference FA value and that from the compared method. These histograms reveal that the proposed reconstruction yields the closest match to the reference grayscale FA map.

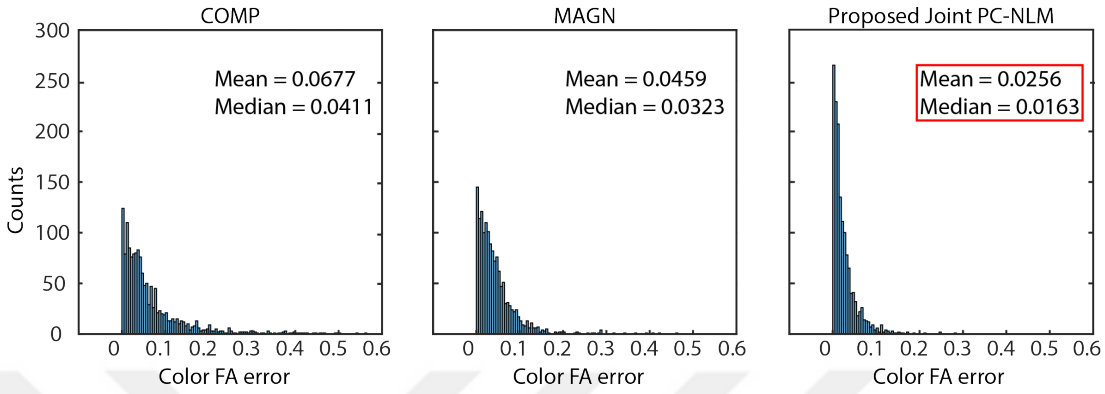

Figure 4.4: Histograms of the color-coded FA errors (with respect to the reference simulated data). The color-coded FA error is measured as the Euclidean distance between the principle eigenvector in the color FA map of the reference data and that of the compared method. These histograms reveal that the proposed reconstruction yields the closest match to the reference color-coded FA map.

4.6 In vivo Experiment Results

Figure 4.5 displays the in vivo imaging results in the spinal cord for isotropic DWI and the most problematic direction. Yellow arrows show the local signal cancellations in COMP. MAGN, on the other hand, does not suffer from this local signal problem, but yields a washed-out look and noise accumulation. The proposed reconstruction does not suffer from local signal cancellations, while preserving the image quality.

The grayscale and color-coded FA map results are shown in Fig. 4.6. The noise accumulation in the background is prominent in the case of MAGN. COMP yields local signal cancellations, which can lead to inaccurate estimation of the principal diffusion direction as clearly seen in color-coded FA maps. The proposed reconstruction not only supressed the noise at the background, it is free from the signal cancellations as well.

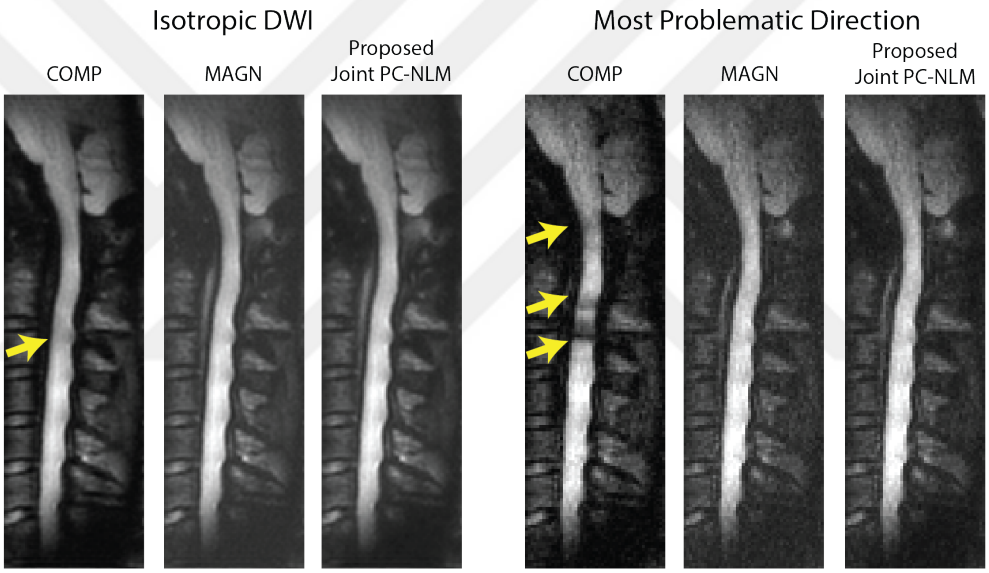

Figure 4.5: Isotropic DWI images and the DWI images from the most problematic direction (i.e., A/P direction). The isotropic DWI images show reduced sensitivity against noise and signal cancellations, as all diffusion directions are utilized to form these images. On the other hand, yellow arrows in the most problematic direction ($[G_{SI}, G_{AP}, G_{RL}] = [0\,1\,0]$), depict the severe local signal cancellations in COMP. In MAGN, see the noise accumulation at the background. The proposed joint PC-NLM yields an image without any noise accumulation and local signal cancellations.

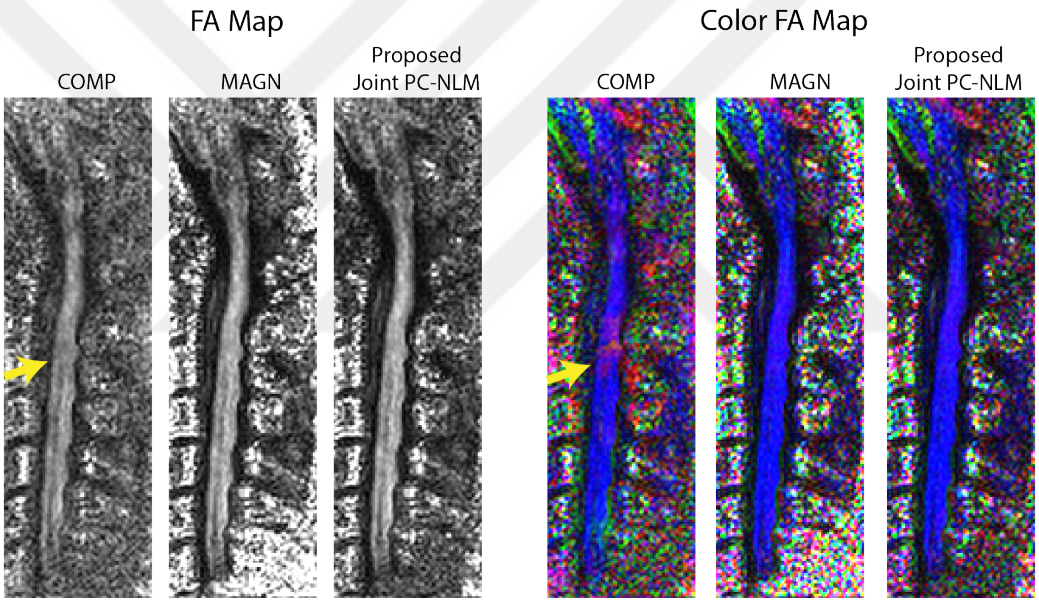

Figure 4.6: Grayscale and color-coded FA maps of all reconstruction techniques. MAGN causes a noise accumulation in the background in both of the FA maps. COMP results in local problems that are especially prominent in the color-coded FA map, as diffusion-direction dependent phase cancellations lead to incorrect estimation of the principle diffusion direction. Again, the proposed reconstruction overcomes the local phase problems while reducing the noise in the FA maps.

Chapter 5

Discussion and Conclusion

High-resolution diffusion MRI is intrinsically SNR-starved. While complex averaging of multiple acquisitions offers improved noise suppression when compared to magnitude averaging, phase errors among multiple acquisitions lead to signal cancellations in combined images. It is observed that these signal cancellations are prominent in the spinal cord where substantial local motion is present along the A/P direction. To the best of our knowledge, this local-motion-induced signal cancellation problem in the spinal cord has not been reported in the literature previously. Several factors might have contributed to this problem remaining elusive in clinical settings. First, diffusion MRI acquisitions are most commonly performed in the brain where local motion may not be as problematic as in the spinal cord. Second, the majority of diffusion MRI acquisitions are performed using ss-EPI followed by magnitude averaging across acquisitions. Lastly, even in the case of complex averaging, the described signal cancellation problem is encountered in a subset of the subjects that have been imaged during our studies. The relative infrequency of this problem makes it all the more important that it should be avoided, as signal cancellation may otherwise be mistaken for increased diffusion due to pathology.

The proposed reconstruction scheme incorporates a new PC-NLM filter for DWI and DTI that increases the image SNR via averaging across pixels with

highly similar patches. Importantly, the search for similar patches takes into account both the magnitudes and the phases of the patch pixels. While a few of the previous studies applied denoising on complex diffusion MRI data, they were restricted to single acquisitions (i.e., no repetitions to average) [50, 51]. Here,the proposed PC-NLM filter performs averaging to simultaneously suppress signal cancellations due to phase errors and reduce noise amplification. Our PC-NLM for DWI results demonstrate that, when NSR$\geq$0.125, the proposed reconstruction achieves higher PSNR and SSIM values than methods based on magnitude averaging. In addition, it yields comparable image quality to methods based on complex averaging, but without signal cancellation artifacts.

While performing PC-NLM for DWI, image quality analyses for additional comparison techniques revealed that the PC-NLM for DWI has superior image quality. When compared to Rician noise model fitting, the proposed reconstruction has higher PSNR and SSIM for NSR$\geq$ 0.100, while providing reliable ADC values even in low SNR regions. The problems of model fitting are exacerbated at low SNR cases and especially for fewer NEXs, as shown in Fig. 3.10. This result is expected, as model fitting becomes increasingly challenging with fewer samples to fit. Another problem of model fitting is that it assumes the magnitude DWI images to follow a Rice distribution. In reality, however, both refocusing and partial k-space reconstructions remove slowly varying phase information from images. In addition, partial k-space reconstruction fills the missing half of k-space using the acquired part. These processes cause the complex noise to deviate from a white Gaussian distribution, and thereby cause the magnitude DWI images to deviate from a Rice distribution. As such, in pixels where the signal and std of noise are comparable, ML estimation can fail to find a non-negative fit for the true signal intensity. Here a small albeit non-zero value of $\sigma_g/100$ is assigned to those pixels. Then, ADC can be under or overestimated depending on how the assigned value compares with the true signal intensity. Yet this procedure is preferable to assigning a zero value that would yield infinitely large ADC estimations. In contrast to these problems of model fitting, PC-NLM provides visually improved image quality even at reduced number of acquisitions, yielding reliable ADC estimates and successfully avoiding signal cancellation artifacts.

Signal cancellation artifacts due to motion-induced phase errors may also be mitigated to a certain extent with cardiac gating, if the cardiac synchronization is optimized to acquire the data at the periods of relative quiescence (e.g., starting approximately $320ms$ after the cardiac trigger signal) [52]. This approach may especially be useful for multi-shot acquisitions to alleviate phase inconsistencies among interleaved data, where the proposed method cannot be used in its current form. Although gating was not performed for the single-shot multiple-NEX in vivo data in this study, utilizing a cardiac-gated acquisition can further increase the performance of the proposed reconstruction. It should be noted that cardiac-gating based approaches prolong the scan time considerably, especially when multiple averages are needed to increase the SNR. PC-NLM solves the signal cancellation issue while increasing the SNR, without the expense of prolonged scan time. A potential limitation of both versions of the proposed reconstruction relates to the trade-off between noise suppression and spatial resolution, inherent to filtering. One way to mitigate resolution loss is to restrict the smoothing parameter to small values. Note that the smoothing parameter directly affects image quality, as well as the tolerance to magnitude differences and phase errors among neighborhoods. As the smoothing parameter increases, magnitude and phase differences become more tolerable, causing increased averaging and thereby blurring in the final image. To minimize potential losses in resolution, the smoothing parameter is computed prior to the POCS step that can amplify high frequency noise. β is set to 0.5, as typically done to minimize resolution loss in low-noise cases [20]. When reconstructions were performed with $\beta = 1$ instead, excessive image blurring occurred (results not shown). In future work, one of the plans is to investigate the benefits of spatially-adaptive selection of the smoothing parameter based on local SNR variations in the image (e.g., due to locally-varying coil sensitivities) [11]. This approach could better preserve resolution in high-SNR regions like the pons or cerebellum, while successfully denoising regions with lower coil sensitivities such as the inferior cervical spine.

In spinal cord imaging, novel approaches that apply high b-value and/or axial acquisitions with NEX= 1 are emerging [48,53–56]. Since PC-NLM targets multi-acquisition imaging, it does not have a direct application for NEX= 1 cases.

Nevertheless, the phase issues described in this work should inform the handling and acquisition of interleaved data. Note that ss-EPI with multiple acquisitions is still the most frequently used sequence in clinical settings. While this work especially targeted that sequence, given its robustness against reduced SNR, PC-NLM is expected to perform equally well for high b-value imaging. For axial imaging of the spinal cord, a potentially uniform phase over the cord is expected, varying across acquisitions. Note that the phase over the cord would still be different than that of the background tissue, creating similar signal cancellation problems that might be overcome with the proposed PC-NLM reconstruction. In vivo demonstration of PC-NLM for non-sagittal orientations remains a future work.

In this thesis, NLM filtering for spinal cord DWI is examined unlike most of the prior work on NLM that focused on brain imaging. It could be hypothesized that morphological differences between the two anatomies might alter NLM's overall efficacy. Yet, the neighborhood size and search volume parameters for PC-NLM are set to$d = 1$ and $M = 5$ based on previously shown optimum values for NLM in the brain [20]. When different values of d and M are tested in the simulation framework for spinal cord DWI, it is found that the image quality degrades with larger values of d, and the algorithm is nearly insensitive to changes in M (results not shown). These observations fully agree with those in [20]. The strong agreement between our observations and the reports in Ref. [20] could be attributed to a trade-off between the pixel count and signal heterogeneity. On the one hand, the pixel count is greater in the brain especially when compared to reduced-FOV spinal images. This potentially leads to a smaller number of similar patches to average in the spinal cord. On the other hand, the brain features a variety of different structures when compared to the homogeneous appearance of the spinal cord. In turn, the number of patches to average are increased in the spinal cord. Our results indicate that these two counteracting factors balance each other to yield consistent NLM performance in the brain and the spinal cord.

For DTI and connectivity analyses, signal cancellations can alter the FA maps, which in turn can lead to incorrect estimation of the principle diffusion direction. In such cases, the proposed joint PC-NLM that takes into account the images

from all diffusion directions improve the quality of the FA maps. While a preliminary analysis of this problem is presented in this thesis [57], a detailed analysis that demonstrates the effects of the phase errors on the integrity of the FA maps and connectivity measures remains a future work.

In this thesis, a new image reconstruction approach that reduces noise and suppresses signal cancellations due to motion-induced phase in DWI and DTI is proposed. This technique preserves the details of DWI images and improves image quality while yielding accurate ADC and FA maps. Extensive simulations and in vivo diffusion MRI in the spinal cord of healthy subjects demonstrate the improved performance of the proposed technique over both magnitude averaging and complex averaging following global phase correction.

Bibliography

[1] O. Dietrich, A. Biffar, A. Baur-Melnyk, and M. F. Reiser, "Technical aspects of MR diffusion imaging of the body," *European Journal of Radiology*, vol. 76, no. 3, pp. 314–322, 2010.

[2] D. Le Bihan, J. F. Mangin, C. Poupon, C. Clark, S. Pappata, N. Molko, and H. Chabriat, "Diffusion tensor imaging: concepts and applications." *Journal of Magnetic Resonance Imaging*, vol. 13, no. 4, pp. 534–46, 2001. [Online]. Available: http://www.ncbi.nlm.nih.gov/pubmed/11276097

[3] J.-D. Tournier, S. Mori, and A. Leemans, "Diffusion tensor imaging and beyond," *Magnetic Resonance in Medicine*, vol. 65, no. 6, pp. 1532–1556, 2011. [Online]. Available: http://doi.wiley.com/10.1002/mrm.22924

[4] R. Bammer and F. Fazekas, "Diffusion imaging of the human spinal cord and the vertebral column." *Topics in Magnetic Resonance Imaging*, vol. 14, no. 6, pp. 461–476, 2003.

[5] A. W. Anderson and J. C. Gore, "Analysis and correction of motion artifacts in diffusion weighted imaging." *Magnetic Resonance in Medicine*, vol. 32, pp. 379–387, 1994.

[6] O. Dietrich, S. Heiland, and K. Sartor, "Noise correction for the exact determination of apparent diffusion coefficients at low SNR," *Magnetic Resonance in Medicine*, vol. 45, no. 3, pp. 448–453, 2001.

[7] F. Lam, S. D. Babacan, J. P. Haldar, M. W. Weiner, N. Schuff, and Z. P. Liang, "Denoising diffusion-weighted magnitude MR images using rank and

edge constraints," *Magnetic Resonance in Medicine*, vol. 71, no. 3, pp. 1272–1284, 2014.

[8] A. Kristoffersen, "Diffusion measurements and diffusion tensor imaging with noisy magnitude data," *Journal of Magnetic Resonance Imaging*, vol. 29, no. 1, pp. 237–241, 2009.

[9] M. Descoteaux, N. Wiest-daessl, S. Prima, C. Barillot, M. Descoteaux, N. Wiest-daessl, S. Prima, C. Barillot, and R. Deriche, "Impact of Rician Adapted Non-Local Means Filtering on HARDI," *International Conference on Medical Image Computing and Computer-Assisted Intervention*, pp. 122–130, 2008.

[10] J. V. Manjon, N. A. Thacker, J. J. Lull, G. Garcia-Marti, L. Marti-Bonmati, and M. Robles, "Multicomponent MR image denoising," *International Journal of Biomedical Imaging*, 2009.

[11] J. V. Manjon, P. Coupe, L. Marti-Bonmati, D. L. Collins, and M. Robles, "Adaptive non-local means denoising of MR images with spatially varying noise levels," *Journal of Magnetic Resonance Imaging*, vol. 31, no. 1, pp. 192–203, 2010.

[12] N. Wiest-Daesslé, S. Prima, P. Coupé, S. P. Morrissey, and C. Barillot, "Rician noise removal by non-local means filtering for low signal-to-noise ratio MRI: Applications to DT-MRI," *International Conference on Medical Image Computing and Computer-Assisted Intervention*, no. PART 2, pp. 171–179, 2008.

[13] S. Basu, T. Fletcher, and R. Whitaker, "Rician noise removal in diffusion tensor MRI," *Medical Image Computing and Computer-Assisted Intervention*, vol. 9, pp. 117–125, 2006.

[14] S. Aja-Fernandez, M. Niethammer, M. Kubicki, M. E. Shenton, and C. F. Westin, "Restoration of DWI data using a rician LMMSE estimator," *IEEE Transactions on Medical Imaging*, vol. 27, no. 10, pp. 1389–1403, 2008.

[15] S. Aja-Fernandez, C. Alberola-Lopez, and C. F. Westin, "Noise and signal estimation in magnitude MRI and Rician distributed images: A LMMSE approach," *IEEE Transactions on Image Processing*, vol. 17, no. 8, pp. 1383–1398, 2008.

[16] A. Tristan-Vega and S. Aja-Fernandez, "DWI filtering using joint information for DTI and HARDI," *Medical Image Analysis*, vol. 14, no. 2, pp. 205–218, 2010. [Online]. Available: http://dx.doi.org/10.1016/j.media.2009.11.001

[17] K. Krissian and S. Aja-Fernandez, "Noise-driven anisotropic diffusion filtering of MRI," *IEEE Transactions on Image Processing*, vol. 18, no. 10, pp. 2265–2274, 2009.

[18] Z. Ding, J. C. Gore, and A. W. Anderson, "Reduction of noise in diffusion tensor images using anisotropic smoothing," *Magnetic Resonance in Medicine*, vol. 53, no. 2, pp. 485–490, 2005.

[19] T. McGraw, B. Vemuri, E. Özarslan, Y. Chen, and T. Mareci, "Variational denoising of diffusion weighted MRI," *Inverse Problems and Imaging*, vol. 3, no. 4, pp. 625–648, 2009.

[20] P. Coupe, P. Yger, S. Prima, P. Hellier, and C. Kervrann, "An Optimized Blockwise Non Local Means Denoising Filter for 3D Magnetic Resonance Images," *IEEE Transactions on Medical Imaging*, vol. 27, no. 4, pp. 425–441, 2007.

[21] R. D. Nowak, "Wavelet-based Rician noise removal for magnetic resonance imaging," *IEEE Transactions on Image Processing*, vol. 8, no. 10, pp. 1408–1419, 1999.

[22] K. L. Miller and J. M. Pauly, "Nonlinear phase correction for navigated diffusion imaging," *Magnetic Resonance in Medicine*, vol. 50, no. 2, pp. 343–353, 2003.

[23] J. G. Pipe, V. G. Farthing, and K. P. Forbes, "Multishot diffusion-weighted FSE using PROPELLER MRI," *Magnetic Resonance in Medicine*, vol. 47, no. 1, pp. 42–52, 2002.

[24] M. Aksoy, S. Skare, S. Holdsworth, and R. Bammer, "Effects of motion and b-matrix correction for high resolution DTI with short-axis PROPELLER-EPI," *NMR in Biomedicine*, vol. 23, no. 7, pp. 794–802, 2010.

[25] D. A. Porter and R. M. Heidemann, "High resolution diffusion-weighted imaging using readout-segmented echo-planar imaging, parallel imaging and a two-dimensional navigator-based reacquisition," *Magnetic Resonance in Medicine*, vol. 62, no. 2, pp. 468–475, 2009.

[26] C. Liu, M. E. Moseley, and R. Bammer, "Simultaneous phase correction and SENSE reconstruction for navigated multi-shot DWI with non-cartesian k-space sampling," *Magnetic Resonance in Medicine*, vol. 54, no. 6, pp. 1412–1422, 2005.

[27] M. Aksoy, C. Forman, M. Straka, S. Skare, S. Holdsworth, J. Hornegger, and R. Bammer, "Real-time optical motion correction for diffusion tensor imaging," *Magnetic Resonance in Medicine*, vol. 66, no. 2, pp. 366–378, 2011.

[28] M. Aksoy, C. Forman, M. Straka, T. Çukur, J. Hornegger, and R. Bammer, "Hybrid prospective and retrospective head motion correction to mitigate cross-calibration errors," *Magnetic Resonance in Medicine*, vol. 67, no. 5, pp. 1237–1251, 2012.

[29] M. Herbst, J. MacLaren, M. Weigel, J. Korvink, J. Hennig, and M. Zaitsev, "Prospective motion correction with continuous gradient updates in diffusion weighted imaging," *Magnetic Resonance in Medicine*, vol. 67, no. 2, pp. 326–338, 2012.

[30] M. A. Bernstein, K. F. King, and X. J. Zhou, *Handbook of MRI Pulse Sequences*, 2004.

[31] R. Bammer, "Basic principles of diffusion-weighted imaging," *European Journal of Radiology*, vol. 45, no. 3, pp. 169–184, 2003.

[32] E. U. Saritas, J. H. Lee, and D. G. Nishimura, "SNR dependence of optimal parameters for apparent diffusion coefficient measurements," *IEEE Transactions on Medical Imaging*, vol. 30, no. 2, pp. 424–437, 2011.

[33] J. Helenius, L. Soinne, J. Perkiö, O. Salonen, A. Kangasmäki, M. Kaste, R. A. D. Carano, H. J. Aronen, and T. Tatlisumak, "Diffusion-weighted MR imaging in normal human brains in various age groups," *American Journal of Neuroradiology*, vol. 23, no. 2, pp. 194–199, 2002. [Online]. Available: papers3://publication/uuid/98711011-482C-482D-B2FE-457BD170E3B1

[34] C. R. Figley and P. W. Stroman, "Investigation of human cervical and upper thoracic spinal cord motion: Implications for imaging spinal cord structure and function," *Magnetic Resonance in Medicine*, vol. 58, no. 1, pp. 185–189, 2007.

[35] H. Matsuzaki, K. Wakabayashi, K. Ishihara, H. Ishikawa, H. Kawabata, and T. Onomura, "The origin and significance of spinal cord pulsation." *Spinal cord : the official journal of the International Medical Society of Paraplegia*, vol. 34, pp. 422–426, 1996.

[36] S. Winklhofer, F. Schoth, P. Stolzmann, T. Krings, M. Mull, M. Wiesmann, and C. P. Stracke, "Spinal Cord Motion: Influence of Respiration and Cardiac Cycle," *RöFo-Fortschritte auf dem Gebiet der Röntgenstrahlen und der bildgebenden Verfahren. Georg Thieme Verlag KG*, vol. 186, no. 11, pp. 1016–1021, 2014.

[37] X. Zhong, C. H. Meyer, D. J. Schlesinger, J. P. Sheehan, F. H. Epstein, J. M. Larner, S. H. Benedict, P. W. Read, K. Sheng, and J. Cai, "Tracking brain motion during the cardiac cycle using spiral cine-DENSE MRI." *Medical physics*, vol. 36, no. 8, pp. 3413–3419, 2009.

[38] A. Buades, B. Coll, and J.-M. Morel, "A Review of Image Denoising Algorithms, with a New One," *Multiscale Modeling & Simulation*, vol. 66, no. 4, pp. 1383–1406, 2006.

[39] J. Boulanger, C. Kervrann, and P. Bouthemy, "Adaptive spatio-temporal restoration for 4D fluorescence microscopic imaging," *International Conference on Medical Image Computing and Computer-Assisted Intervention*, vol. 3749 LNCS, pp. 893–901, 2005.

[40] T. Gasser, L. Sroka, and J.-S. Christine, "Residual variance and residual pattern in nonlinear regression," *Biometrika Trust*, vol. 73, no. 3, pp. 625–633, 1986.

[41] E. M. Haacke, E. D. Lindskogj, and W. Lin, "A fast, iterative, partial-fourier technique capable of local phase recovery," *Journal of Magnetic Resonance*, vol. 92, no. 1, pp. 126–145, 1991.

[42] B. De Leener, J. Cohen-Adad, and S. Kadoury, "Automatic Segmentation of the Spinal Cord and Spinal Canal Coupled with Vertebral Labeling," *IEEE Transactions on Medical Imaging*, vol. 34, no. 8, pp. 1705–1718, 2015.

[43] V. S. Fonov, A. Le Troter, M. Taso, B. De Leener, G. Lévêque, M. Benhamou, M. Sdika, H. Benali, P. F. Pradat, D. L. Collins, V. Callot, and J. Cohen-Adad, "Framework for integrated MRI average of the spinal cord white and gray matter: The MNI-Poly-AMU template," *NeuroImage*, vol. 102, no. P2, pp. 817–827, 2014. [Online]. Available: http://dx.doi.org/10.1016/j.neuroimage.2014.08.057

[44] C. B. G. T. B. Clark, "Magnetic Resonance Diffusion Imaging of the Human Cervical Spinal Cord in vivo," *Proceedings of the International Society for Magnetic Resonance in Medicine*, no. s1, pp. 1152–1161, 1998.

[45] E. U. Saritas, C. H. Cunningham, J. H. Lee, E. T. Han, and D. G. Nishimura, "DWI of the spinal cord with reduced FOV single-shot EPI," *Magnetic Resonance in Medicine*, vol. 60, no. 2, pp. 468–473, 2008.

[46] H. Gudbjartsson and S. Patz, "The Rician Distribution of Noisy MRI Data," *Magnetic Resonance in Medicine*, pp. 910–914, 1995.

[47] C. G. Koay and P. J. Basser, "Analytically exact correction scheme for signal extraction from noisy magnitude MR signals," *Journal of Magnetic Resonance*, vol. 179, no. 2, pp. 317–322, 2006.

[48] F. Grussu, T. Schneider, H. Zhang, D. C. Alexander, and C. A. M. Wheeler-Kingshott, "Neurite orientation dispersion and density imaging of the healthy cervical spinal cord in vivo," *NeuroImage*, vol. 111, pp. 590–601, 2015. [Online]. Available: http://dx.doi.org/10.1016/j.neuroimage.2015.01.045

[49] Z. Wang, A. C. Bovik, H. R. Sheikh, and E. P. Simoncelli, "Image quality assessment: From error visibility to structural similarity," *IEEE Transactions on Image Processing*, vol. 13, no. 4, pp. 600–612, 2004.

[50] R. Wirestam, A. Bibic, J. Lätt, S. Brockstedt, and F. Ståhlberg, "Denoising of complex MRI data by wavelet-domain filtering: Application to high-b-value diffusion-weighted imaging," *Magnetic Resonance in Medicine*, vol. 56, no. 5, pp. 1114–1120, 2006.

[51] J. P. Haldar, V. J. Wedeen, M. Nezamzadeh, G. Dai, M. W. Weiner, N. Schuff, and Z. P. Liang, "Improved diffusion imaging through SNR-enhancing joint reconstruction," *Magnetic Resonance in Medicine*, vol. 69, no. 1, pp. 277–289, 2013.

[52] P. Summers, P. Staempfli, T. Jaermann, S. Kwiecinski, and S. Kollias, "A preliminary study of the effects of trigger timing on diffusion tensor imaging of the human spinal cord." *AJNR. American journal of neuroradiology*, vol. 27, no. 9, pp. 1952–1961, 2006.

[53] S. By, J. Xu, B. A. Box, F. R. Bagnato, and S. A. Smith, "Application and evaluation of NODDI in the cervical spinal cord of multiple sclerosis patients," *NeuroImage: Clinical*, vol. 15, no. May, pp. 333–342, 2017. [Online]. Available: http://dx.doi.org/10.1016/j.nicl.2017.05.010

[54] T. Duval, S. Lévy, N. Stikov, J. Campbell, A. Mezer, T. Witzel, B. Keil, V. Smith, L. Wald, E. Klawiter, and J. Cohen-Adad, "g-Ratio weighted imaging of the human spinal cord in vivo," *NeuroImage*, vol. 145, no. September 2016, pp. 11–23, 2017. [Online]. Available: http://linkinghub.elsevier.com/retrieve/pii/S1053811916304815

[55] T. Duval, J. A. McNab, K. Setsompop, T. Witzel, T. Schneider, S. Y. Huang, B. Keil, E. C. Klawiter, L. L. Wald, and J. Cohen-Adad, "In vivo mapping of human spinal cord microstructure at 300mT/m," *NeuroImage*, vol. 118, pp. 494–507, 2015. [Online]. Available: http://dx.doi.org/10.1016/j.neuroimage.2015.06.038

[56] J. A. D. Farrell, S. A. Smith, E. M. Gordon-Lipkin, D. S. Reich, P. A. Calabresi, and P. C. M. Van Zijl, "High b-value q-space diffusion-weighted MRI of the human cervical spinal cord in vivo: Feasibility and application to multiple sclerosis," *Magnetic Resonance in Medicine*, vol. 59, no. 5, pp. 1079–1089, 2008.

[57] S. G. Kafali, T. Cukur, and E. U. Saritas, "Joint Non local Means Reconstruction for Correction of Phase Induced Errors in Diffusion Tensor Imaging," *In Proceedings of the 25th Annual Meeting of ISMRM, Hawaii, USA, 2017. Abstract Number 3332.*